2022

Scaling Theory of 3D Magnetic Reconnection X-Line Spreading

Milton Arencibia
West Virginia University, miarencibia@mix.wvu.edu

Scaling Theory of 3D Magnetic Reconnection X-Line Spreading

Milton Arencibia

Dissertation Submitted to
The Eberly College of Arts and Sciences
at West Virginia University
in partial fulfillment of the requirements
for the degree of

Doctor of Philosophy
in
Physics

Paul A. Cassak, Ph.D., Chair
Earl Scime, Ph.D.
Weichao Tu, Ph.D.
Zachariah B. Etienne, Ph.D.

Department of Physics and Astronomy

Morgantown, West Virginia, USA
2022

Keywords: magnetic reconnection, solar flares, magnetotail

Abstract

Scaling Theory of 3D Magnetic Reconnection X-Line Spreading

Milton Arencibia

Magnetic reconnection is fundamental process in plasmas that converts magnetic energy into kinetic and thermal energy via a change in magnetic topology. Magnetic reconnection is known to mediate eruptive solar flares, geomagnetic substorms that create the Northern lights, heating and particle acceleration in controlled fusion devices, and is thought to be an important process in numerous settings in high-energy astrophysics. Classical models of reconnection are two-dimensional (2D), but naturally occurring reconnection is three-dimensional (3D), and a manifestation of the 3D nature is that the x-line where the magnetic field topology changes has a finite extent in the direction normal to the plane of reconnection. The x-line can also elongate or spread over time, and this trait has been observed in the laboratory, Earth's magnetosphere, and is thought to be related to the elongation of chromospheric ribbons during solar flares. This dissertation presents a first-principles scaling theory of the three-dimensional spreading of quasi-2D magnetic reconnection of finite extent in the out of plane direction. This theory addresses systems with or without an out of plane (guide) magnetic field, with or without Hall physics, in current sheets with thicknesses that are both uniform and non-uniform in the out of plane direction. The theory reproduces known spreading speeds and directions with and without guide fields, unifying previous knowledge in a single theory, along with new results: (1) Reconnection spreads in a particular direction if an x-line is induced at the interface between reconnecting and non-reconnecting regions, which is controlled by the out of plane gradient of the electric field in the outflow direction. (2) The theory explains why anti-parallel reconnection in resistive-magnetohydrodynamics does not spread. (3) Numerical simulations of anti-parallel reconnection initiated with a pressure pulse instead of a magnetic perturbation suggest magnetosonic waves do not play a role in the propagation of quasi-2D anti-parallel reconnection, as had previously been speculated. (4) In current sheets of non-uniform thickness, when anti-parallel reconnection spreads from a thinner to a thicker region of a current sheet, the spreading speed is both sub-Alfvénic and slower than the speed of the local current carriers predicted for a uniform current sheet of equivalent local thickness; this is due to the initial reconnecting magnetic field being effectively reduced. We confirm these results using 3D two-fluid and resistive-magnetohydrodynamics simulations. The result can be used to predict the time scale of reconnection spreading in Earth's magnetotail, where the near Earth cross-tail current sheet has a thickness that varies along the dawn-dusk direction. It is also potentially important for understanding observations of two-ribbon solar flares and dayside magnetopause reconnection in which reconnection spreads at sub-Alfvénic and sub-current carrier speeds.

Acknowledgements

I would like to express my gratitude to everyone that has played a role in my development as a physicist. I thank Santiago Ramón Guerra Guillén who inspired me to switch majors to physics after countless stimulating conversations about quantum entanglement, Prof. Basilio Ruiz Cobo and Prof. Kinwah Wu, for taking me under their wing for my first research experiences, and the Spanish Ministry of Education for supporting me in my studies.

As for my tenure at WVU, I thank Prof. Maura McLaughlin and Prof. Loren Anderson for communicating my acceptance to the graduate program, Prof. Sean McWilliams for giving me my first experience with graduate level research, and Nathan Garver-Daniels for graciously hosting me at his residence when I first arrived. Immense gratitude goes to my Ph.D. advisor Prof. Paul Cassak for his masterful instruction that always brought the best work out of me and I thank him for believing in my results when my confidence faltered. I also thank my Ph.D. committee members: Prof. Earl Scime, Prof. Weichao Tu, and Prof. Zach Etienne, whom have always offered insightful comments and questions. A special thank you to Prof. Michael Shay, Dr. Steven Petrinec, Prof. Eric Priest, Prof. Jiong Qiu, Dr. Haoming Liang and Prof. Ying Lou for their collaboration which markedly improved the quality of my research.

I would also like to thank my friends and colleagues at WVU and the wider community for enriching my life over the years: Matt Beidler, Mahmud Hasan Barbhuiya, Tom Steinberger, Pedram Tavadze, Arturo Hernandez, Derek Thompson, Drew Elliot, Belinda Cheeseboro, Amber Kiana, Adam Payne, Jeff Walker, and John McKee.

Finally I thank Karla McGraw for her emotional support (and patience!) and my mother Irma for supporting me with my goals.

Table of Contents

List of Tables

List of Figures

Chapter 1

Introduction

1.1 History and Relevance of Magnetic Reconnection

Over 99% of visible matter in the universe is in the plasma state, a highly conducting ionized fluid with behavior dominated by electromagnetic forces. Most of it is found in the form of stars and interstellar clouds, however one not does need to travel cosmic distances to find examples. The outermost envelope of Earth's atmosphere - the magnetosphere - is a plasma threaded by the magnetic field generated by the motions of Earth's fluid metal interior. Earth is itself is immersed in the magnetosphere of the Sun, and the interface between the magnetospheres of the Earth and Sun leads to complicated interactions and a wealth of natural phenomena dubbed "space weather", ranging from the benign and stunning aurora borealis, to particle showers that can endanger astronauts and damage spacecraft, disrupt telecommunications and destroy ground-based electrical infrastructure.

In a magnetized plasma, two domains of magnetic field with a component that is oppositely directed coming into proximity form a thin current sheet along the magnetic null surface (along which the net magnetic field is zero) separating the domains. Under these conditions, cross-connections of the oppositely directed fields may take place at a point known as the x-line, causing a quick relaxation of the magnetic field that accelerates plasma out of the current sheet. This process

is known as magnetic reconnection and it effectively converts magnetic energy into kinetic and thermal plasma energy through a change in magnetic topology (Dungey, 1953; Vasyliunas, 1975).

An early conception of magnetic reconnection appeared in the late 1940's (Giovanelli, 1950; Lockwood, 2016) in which acceleration of particles at magnetic nulls were proposed as the mechanism behind eruptive solar flares, fast bursts of radiation often coupled with expulsions of matter from the outer solar atmosphere or "corona", releasing energies as high as $10^{26}J$ in seconds (Russell et al., 2015). Quantitative models of magnetic reconnection were developed later (Dungey, 1953; Parker, 1957; Sweet, 1958; Petschek, 1964a) and will be discussed in detail in Sec. (1.2). An exceptionally powerful example of a solar flare that occurred on April 2nd 2001 is shown in Fig. 1.1, showing the enhanced brightening from the flare on the Eastern limb of the Sun, and above it the resulting "coronal mass ejection" (CME) launching plasma at approximately 7.2 million kilometers per hour into interplanetary space.

A qualitative understanding of solar flares can be gained from the "standard model" of solar flares, also known as the CSHKP model (Carmichael, 1964; Sturrock, 1966; Hirayama, 1974; Kopp & Pneuman, 1976), which explains the observable features of flares on the basis of magnetic reconnection occurring in the corona. Figure 1.2 shows a sketch of the model with one of many possible configurations of the magnetic field in the corona that can lead to eruptive "two-ribbon" solar flares. In this model, loops of coronal magnetic field that stretch $\sim 10Mm$ above the solar surface or "photosphere" become unstable and reconnect, forming a thin current sheet in the green box where the magnetic field changes direction. The end result

is that the plasma trapped along the magnetic field lines is launched upwards into interplanetary space in the form of a CME, the blob-like structure at the top of the coronal field loop.

Reconnection in the corona also expels plasma along the newly reconnected loops, traveling downwards through increasingly denser layers of the solar atmosphere, the "chromosphere" and ultimately the photosphere. The deceleration of the reconnection exhaust through the chromosphere produces bright pairs of "ribbons" at the footpoints of the coronal magnetic field. These ribbons are observed as Hα emission (optical emission from atomic hydrogen at a wavelength of 656nm) and are accompanied with X-ray and extreme ultraviolet (EUV) emission from the newly reconnected magnetic field loops ("hot flare loops"). An example of an observation of flare ribbons is shown in Fig. 1.3. Panels (a)-(f) show the temporal evolution of a pair of flare ribbons in three separate wavelengths at two different times, showing their expansion and elongation along the inferred direction of the magnetic polarity inversion line (PIL) separating opposing magnetic field polarities at the estimated loop top height, depicted as a white line in panels (e) and (f). Panels (c) and (f) show the sequential appearance of newly reconnected hot flare loops (see Fig. 1.2), suggesting an elongation of reconnection from its original location A to location B along the PIL. Panel (g) is a magnetogram superimposed with newly formed ribbons with a color scale that represents time evolution progressing from violet to red in minutes, showing both the expansion of the ribbons outward from the PIL and their progressive elongation along the PIL, with the orange arrow representing the inferred direction of the macroscopic electric current in the corona. Panels (h) and

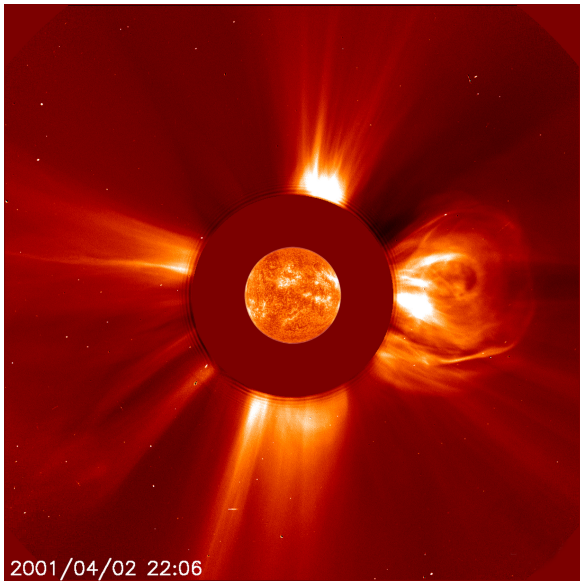

Figure 1.1 Composite image of a large solar flare, showing enhanced brightening on the Eastern limb of the Sun, along with a coronal mass ejection directly above (the emerging loop-like structure on the far right). Picture credit: SOHO/MDI, SOHO/EIT, and SOHO/LASCO (ESA & NASA) Special credit: G. Lawrence (LASCO/NRL) for initial data collection and movies.

(i) are time-distance stack plots (where the horizontal axis is time and the vertical axis is distance) of emission from the coronal loop tops in two different wavelengths, where the slopes shown as dashed lines provide a measure of the speed of the spreading of the newly formed hot flare loops which may be thought of as a proxy for the speed of the spreading of reconnection (Qiu et al., 2017).

Shortly after magnetic nulls had been posited as the mechanism powering solar flares, it was speculated that the same process could be responsible for Earth's aurora borealis. This line of study became the PhD research and early career work of Jim Dungey (Dungey, 1953, 1958, 1961), in which the term "magnetic reconnection" was first coined in the literature and in which the currently accepted model of Earth's magnetosphere and geomagnetic storms first appeared. In the Dungey

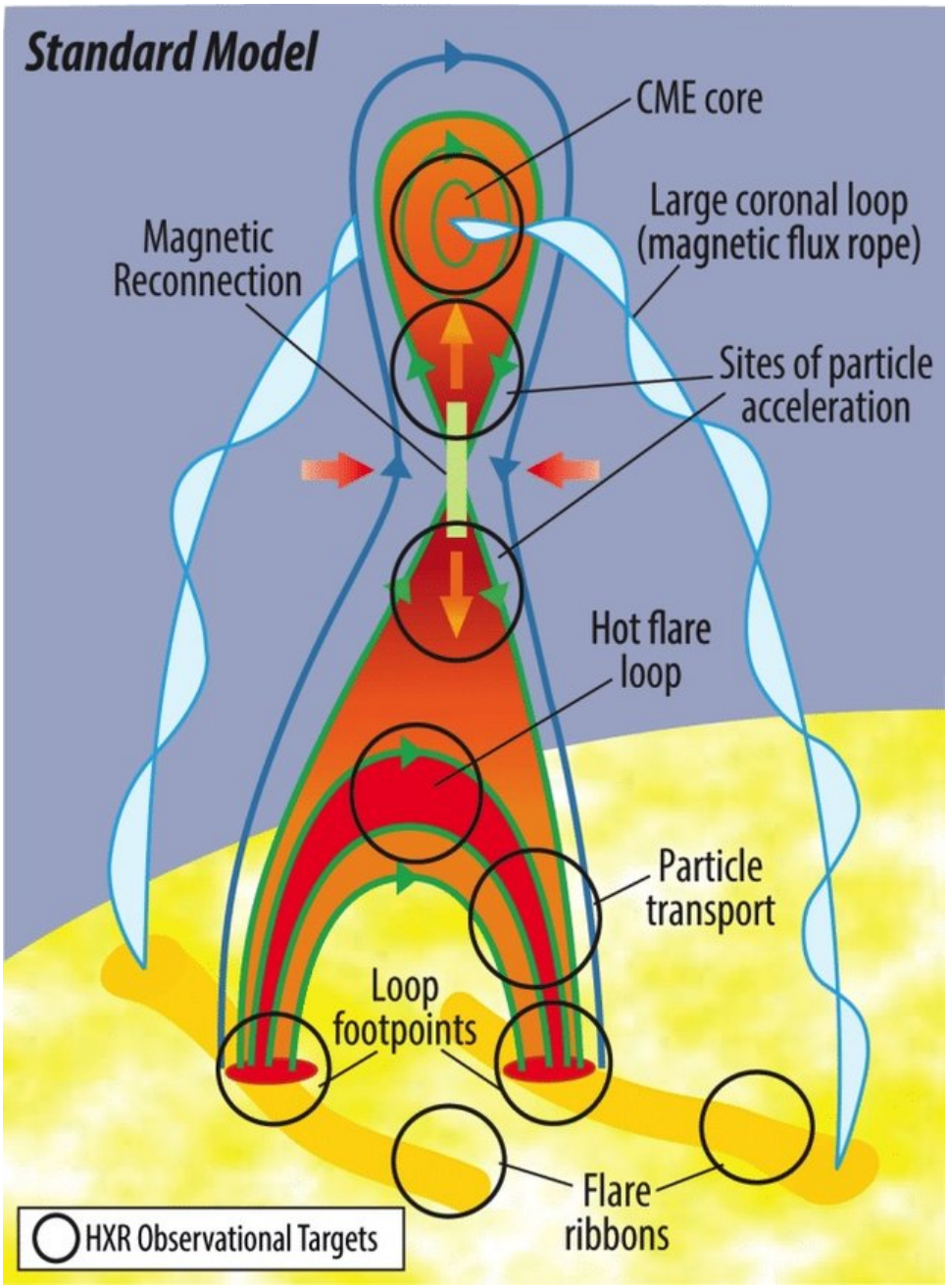

Figure 1.2 Standard CSHKP model of solar flares, describing the observed features of two-ribbon solar flares (chromospheric ribbons and x-ray emission from flare loops) on the basis of magnetic reconnection occurring in the corona. Figure adapted from Shibata et al. (1995). © AAS. Reproduced with permission.

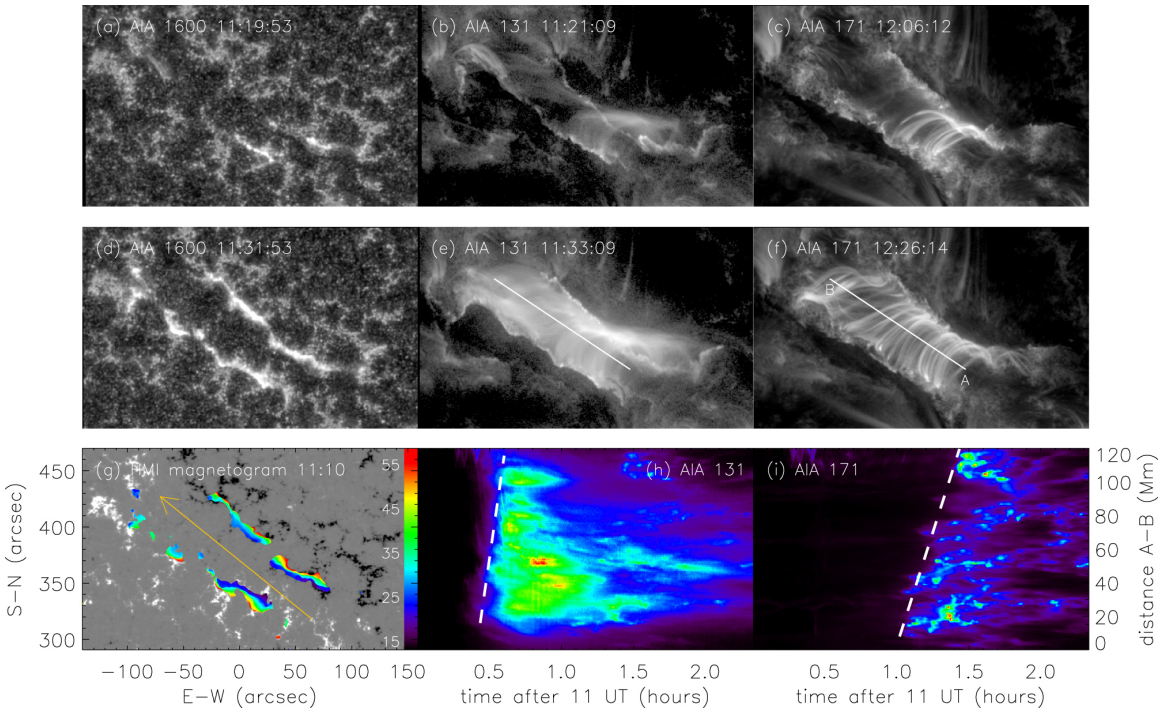

Figure 1.3 (a)–(f): Snapshots of the flare SOL2011-09-13T22 observed at three passbands of AIA during its evolution. (g) Longitudinal magnetogram (grayscale) by HMI superimposed with the positions of newly brightened ribbons (color). Time in minutes from 22:00 UT is indicated by the color code. The orange curve outlines the PIL of the photospheric longitudinal magnetogram, and the arrow indicates the direction of the macroscopic electric current in the corona. (h) Time–distance stack plot of the loop top emission in the EUV 131 passband along the axis of the flare arcade (indicated by the solid white line in panels (e) and (f)). The dashed guide line outlines the front of the spreading loops at an average speed of 13 km s^{-1}. (i) Time–distance stack plot of loop top emission in the EUV 171 passband along the axis of the flare arcade. The dashed guide line outlines the front of the spreading loops at an average speed of 10 km s^{-1}. Original figure and caption credit: Qiu et al. (2017). ©AAS. Reproduced with permission.

model of the magnetosphere sketched in Fig. 1.4, the solar wind coming from the left drags along the coronal magnetic field into interplanetary space dubbed the interplanetary magnetic field (IMF), shown in blue in the far left with a southward orientation The direction of the IMF is variable on the scale of minutes. If a southward IMF collides with Earth's magnetic field (pointing northward at the equator), this results in magnetic reconnection at the dayside boundary between the two called the "magnetopause", forming a x-line shown as the black X in the far left of Fig. 1.4 where the magnetic connectivity changes and plasma is accelerated and heated. The newly reconnected field lines shown in orange are then continually draped towards the nightside of Earth by the solar wind, where they form a long comet-like tail of oppositely directed magnetic fields stretching hundreds of Earth radii. This structure is called the magnetotail and may reconnect again causing a geomagnetic substorm (McPherron, 1970; McPherron et al., 1973), forming another reconnection x-line shown as the black X on the far right, often a few tens of Earth radii away from Earth in the nightside direction (Voigt, 1984; Sergeev et al., 1990). When a substorm takes place, the exhaust from magnetotail reconnection travels down the newly reconnected field lines shown in red towards Earth's magnetic poles, exciting oxygen and nitrogen in the atmosphere, producing the multi-colored glow of the aurora borealis. This is analogous to the chromospheric ribbons that are formed during two-ribbon solar flares (Reeves et al., 2008). Though initially controversial, the Dungey model for geomagnetic storms is now supported by decades of ground-based and in situ spacecraft observations (Kivelson & Russell, 1995; Priest & Forbes, 2000; Cowley FRS, 2015) and a similar process has been observed on

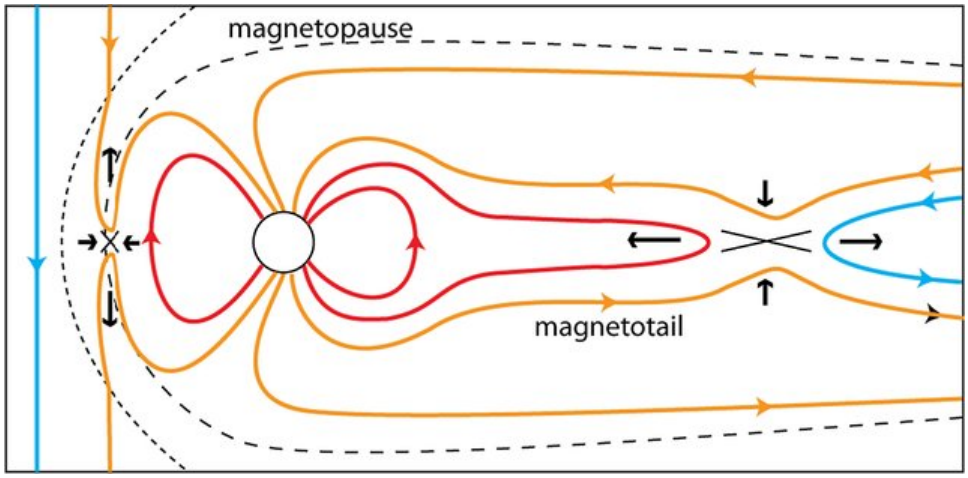

Figure 1.4 A schematic of plasma circulation in the Earth's magnetosphere for southward IMF conditions. As originally proposed by Dungey, magnetic reconnection at the dayside magnetopause and in the magnetotail results in the concept of the open magnetosphere. Reproduced under Creative Commons licensing from Eastwood et al. (2017).
Creative Commons license: https://s100.copyright.com/AppDispatchServlet?title=The%20Scientific%20Foundations%20of%20Forecasting%20Magnetospheric%20Space%20Weather&author=J.%20P.%20Eastwood%20et%20al&contentID=10.1007%2Fs11214-017-0399-8&copyright=The%20Author%28s%29&publication=0038-6308&publicationDate=2017-08-15&publisherName=SpringerNature&orderBeanReset=true&oa=CC%20BY

Mercury (Slavin et al., 2021).

1.2 2D Magnetic Reconnection Theory

1.2.1 Resistive MHD and the Magnetic Diffusion Model

An ideal plasma is a perfect electrical conductor, and thus the simplest fluid description - ideal magnetohydrodynamics (MHD) - does not include resistive effects (arising from electron-ion collisions), or for that matter, any other physics that creates electric fields in the reference frame of the moving plasma, prescribing the magnetic field and plasma motions to be locked in with each other. In ideal MHD,

this condition is known as the "frozen-in flux theorem" (Axford, 1984; Choudhuri, 1998) and it prevents charged particles in the plasma to escape their orbits about the magnetic field and "slip", a requirement for magnetic reconnection. The "classical" theory of two-dimensional reconnection proposed by Dungey (Dungey, 1953, 1958, 1961) provides a solution based on the idea of thin current sheets forming where the magnetic field changes direction with a finite resistivity due to collisions inside the sheet, allowing diffusion of the magnetic field and slippage of the plasma to take place within. Outside of the current sheet, the plasma behaves like a perfect conductor again and ideal MHD approximately holds.

The fluid description of a singly-ionized plasma with finite uniform resistivity is embodied by the resistive-MHD equations, which combines the equations of mass continuity, momentum, and the pressure equation with Faraday's law of induction, Ampere's law in the quasi-static limit (meaning a negligible displacement current), and the resistive Ohm's law from electromagnetism with a number of approximations and simplifying assumptions. In the order mentioned, these equations are in Gaussian (cgs) units:

$$\frac{\partial \rho}{\partial t} + \nabla \cdot (\rho \mathbf{v}) = 0 \tag{1.1}$$

$$\rho \left[\frac{\partial \mathbf{v}}{\partial t} + (\mathbf{v} \cdot \nabla)\mathbf{v} \right] = -\nabla p + \frac{\mathbf{J} \times \mathbf{B}}{c} \tag{1.2}$$

$$\frac{\partial p}{\partial t} + \mathbf{v} \cdot \nabla p = -\gamma p \nabla \cdot \mathbf{v} + (\gamma - 1)\eta J^2 \tag{1.3}$$

$$\frac{\partial \mathbf{B}}{\partial t} = -c\nabla \times \mathbf{E} \tag{1.4}$$

$$\nabla \times \mathbf{B} = \frac{4\pi}{c}\mathbf{J} \tag{1.5}$$

$$\mathbf{E} = -\frac{\mathbf{v} \times \mathbf{B}}{c} + \eta \mathbf{J}, \tag{1.6}$$

where ρ is the plasma density, $\mathbf{v}$ is the center of mass velocity of the plasma ($\mathbf{v} = (m_i n_i \mathbf{v_i} + m_e n_e \mathbf{v_e})/(m_i + m_e) \approx m_i n \mathbf{v_i}$ for $m_i >> m_e$, where m_i, m_e, $\mathbf{v_i}$ and $\mathbf{v_e}$ are the ion and electron masses and fluid velocities respectively), $n \approx n_i \approx n_e$ is the particle density (approximately equal for ions and electrons in quasineutral plasmas), p is the net thermal pressure of the plasma defined as the sum of ion and electron thermal pressures and for simplicity is assumed isotropic (hence a scalar), γ is ratio of specific heats, $\mathbf{J}$ is the net electric current density, $\mathbf{B}$ is the net magnetic field, c is the speed of light, η is the resistivity, and $\mathbf{E}$ is the net electric field. For $\eta = 0$, this set of equations reduces to ideal MHD.

The resistive-MHD model is a valid approximation over spatial scales and time scales larger than those associated with the gyro-orbits of ions and electrons, for non-relativistic velocities, and for quasineutral plasmas with a finite resistivity and negligible viscosity (which may be included if desired). Despite these limitations, the model is sufficient for describing the classic early models of magnetic reconnection (Dungey, 1953; Sweet, 1958; Parker, 1957). If we combine equation 1.4 with 1.6 and assume a uniform resistivity, we obtain the resistive induction equation

$$\frac{\partial \mathbf{B}}{\partial t} = \nabla \times (\mathbf{v} \times \mathbf{B}) + \frac{\eta c^2}{4\pi} \nabla^2 \mathbf{B}. \tag{1.7}$$

This first term on the right hand side (RHS) is the convective term describing the evolution of the magnetic field due to ideal MHD, capturing convection, compression,

and bending of the magnetic field, and the second term is the diffusion term, accounting for resistive diffusion of the magnetic field. We can determine how quickly magnetic diffusion occurs by performing what is known as a "scaling analysis" or order of magnitude estimate, by ignoring the ideal MHD term and solving for the timescale on the LHS of equation 1.7. This is done by approximating all derivatives with constants of the characteristic scales ($\partial t \rightarrow t_d$, $\nabla \rightarrow 1/\delta$, and $\partial \mathbf{B} \rightarrow B$), which gives

$$t_d \sim \frac{4\pi\delta^2}{c\eta} \tag{1.8}$$

which can be thought of as the time t_d it takes for the magnetic field within a current sheet of width δ to be completely annihilated by resistive diffusion. Another useful result from a scaling analysis is the ratio of the induction term to the diffusion term in equation 1.7, which gives a measure of whether convection or diffusion dominates in a system. This ratio is known as the magnetic Reynolds number

$$R_m = \left| \frac{\nabla \times (\mathbf{v} \times \mathbf{B})}{\frac{\eta c^2}{4\pi} \nabla^2 \mathbf{B}} \right| \sim \frac{4\pi v L}{\eta c^2}, \tag{1.9}$$

where v and L are the characteristic speed and length of the system, respectively. For reconnection, the characteristic size of the system is typically taken to be the current sheet length which extends to global scales. When $v = c_A$, the Alfvén wave speed, generated by the restoring force of a bent magnetic field (Alfvén, 1942), this

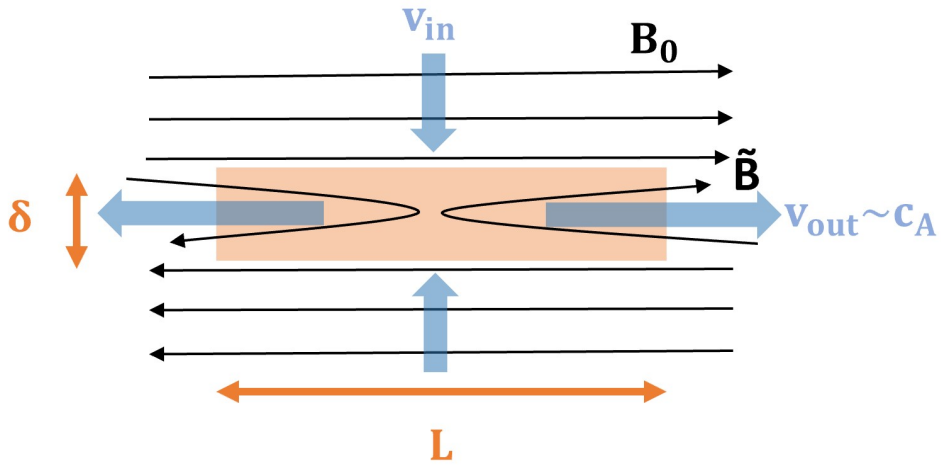

Figure 1.5 Sketch illustrating the Sweet-Parker model of steady-state magnetic reconnection, showing reversed magnetic fields with magnitude B_0 (black arrows) convecting into a resisitve diffusion layer (orange rectangle) at a velocity v_{in} (vertical blue arrows), reconnecting and emerging from the layer at a velocity v_{out} (horizontal blue arrows) with a magnitude $\tilde{B}$.

dimensionless number is called the Lundquist number,

$$S_L = \frac{4\pi c_A L}{\eta c^2}, \tag{1.10}$$

and is related to the rate of collisional reconnection as we will see shortly.

1.2.2 The Sweet-Parker Model of Collisional Reconnection

The question of how magnetic reconnection accelerates plasma in resistive MHD is answered by the Sweet-Parker model (Sweet, 1958; Parker, 1957) sketched in Fig. 1.5, which assumes that oppositely directed magnetic fields with asymptotic magnitude B_0 (depicted as straight black arrows) convect with the plasma at a flow speed v_{in} (blue vertical arrows) into a long collisional current sheet depicted as an orange rectangle with thickness δ and length L set by the global scale of

the system (Birn & Priest, 2007), within which reconnection of field lines takes place. The inflowing plasma is then ejected from the sides of the current sheet at a speed v_{out} (horizontal blue arrows), dragging out the newly reconnected field lines with magnitude $\tilde{B}$ shown as the bent black arrows. This treatment of the model assumes the plasma is incompressible and that reconnection occurs perpetually in a steady-state for simplicity. These assumptions allow us to obtain a constraint on the velocity of plasma flowing into and out of the reconnecting current sheet from a scaling analysis of the continuity equation 1.1. Minding the incompressibility condition ($\nabla \cdot \mathbf{v} = 0$), the resulting scaling relationship is

$$\frac{v_{in}}{v_{out}} \sim \frac{\delta}{L}, \tag{1.11}$$

meaning the aspect ratio of the reconnecting layer δ/L sets the rate at which plasma can flow into and out of the current sheet, putting a limit on the rate of magnetic reconnection. A consequence of the steady-state assumption is that the LHS of Faraday's law (equation 1.4) vanishes, implying the out-of-plane electric field E is spatially uniform and thus we can match the upstream field $E \sim v_{in}B_0/c$ to the field inside the current sheet $E \sim \eta J \sim \eta c B_0/4\pi\delta$ and the downstream electric field $E \sim v_{out}\tilde{B}/c$, giving a constraint on the inflow velocity

$$v_{in} \sim \frac{c^2\eta}{4\pi\delta}, \tag{1.12}$$

as well as on the ratio of the reconnected field $\tilde{B}$ to the reconnecting field B_0 given by

$$\frac{\tilde{B}}{B_0} \sim \frac{v_{in}}{v_{out}} \sim \frac{\delta}{L}. \tag{1.13}$$

Conservation of energy also implies that if magnetic fields of strength B_0 are completely annihilated by reconnection and converted into the bulk kinetic energy of the plasma then $B_0^2/8\pi \sim \frac{1}{2}\rho v_{out}^2$, which imposes a constraint on the outflow velocity given by

$$v_{out} \sim \sqrt{\frac{B_0^2}{4\pi\rho}} = c_A, \tag{1.14}$$

making the reconnection outflow velocity scale with the Alfvén speed of the system based on the reconnecting magnetic field (Parker, 1957). Combining the Sweet-Parker relationships from equations 1.11, 1.12, and 1.13, we obtain a dimensionless rate of reconnection purely in terms of the resistivity and size of the system

$$\frac{v_{in}}{v_{out}} \sim \sqrt{\frac{c^2\eta}{4\pi c_A L}} \sim \frac{1}{\sqrt{S_L}}, \tag{1.15}$$

showing the dependence on the Lundquist number as alluded to earlier. It is also common to express the reconnection rate in terms of the out-of-plane electric field E, since via the integral form of Faraday's law 1.4, it is related to the time rate of change of magnetic flux. This definition, unlike equation 1.15, is independent of resistivity and thus also valid for collisionless reconnection rates, and can also be expressed in a dimensionless form by normalizing to the upstream field and outflow velocity, $E' \sim cE/c_A B_0$.

To demonstrate how reconnection accelerates plasma in the Sweet-Parker model, we combine equation 1.2 with 1.5 to rewrite the momentum equation in a more elucidating form, which after after some vector calculus manipulation is

$$\rho(\mathbf{v}\cdot\nabla)\mathbf{v} = \frac{1}{4\pi}\mathbf{B}\cdot\nabla\mathbf{B} - \nabla\left(\frac{B^2}{8\pi} + p\right) \tag{1.16}$$

where we note the local time derivative $\partial/\partial t$ vanishes in the steady-state. The two terms on the RHS are the magnetic curvature force per unit volume arising from the spatial gradient of the magnetic field in the direction of the net magnetic field and the net (fluid and magnetic) pressure force per unit volume. A newly reconnected magnetic field line is highly curved as shown in Fig. 1.5, with a resulting curvature force that points in the horizontal direction outwards from the current sheet. Adopting x and y as the outflow and inflow directions, balancing the inertia and curvature force in the x-component of equation 1.16 gives the scaling relationship

$$\rho v_x \frac{\partial v_x}{\partial x} \sim \frac{1}{4\pi} B_y \frac{\partial B_x}{\partial y} \tag{1.17}$$

showing that the magnetic curvature force produces horizontal acceleration of the plasma out of the current layer. The final velocity of the plasma exiting the layer can again be shown to scale with the Alfvén speed $c_A = B_0/\sqrt{4\pi\rho}$ based on the upstream field B_0, given the scalings $\rho v_x \partial v_x/\partial x \sim \rho v_{out}^2/L$ and $(B_y/4\pi)\partial B_x/\partial y \sim \tilde{B}B_0/4\pi\delta \sim B_0^2/4\pi L$ (using equation 1.12), consistent with our earlier argument from energy conservation.

An unfortunate downside of the Dungey diffusion and Sweet-Parker models is that they are much too slow to explain the quick timescales for energy release in typical solar flares. This can be made evident by rewriting the scaling equation 1.11 in terms of transit times instead of velocities, *i.e.*, the Alfvén crossing time $t_A = L/c_A$ for an Alfvén wave to cross the length of the system. We find that the time scale for reconnection is, after rearranging,

$$t_{SP} \sim \sqrt{S_L} t_A, \tag{1.18}$$

where $t_{SP} = L/v_{in}$ is the "Sweet-Parker timescale". The Alfvén crossing time in the solar corona is on the order of 10 seconds, using $L \approx 10^7$ m for the coronal magnetic field loop height and $c_A \approx 10^6$ m/s (Qiu et al., 2017). A typical Lundquist number in the corona is $\approx 10^9$ or larger (Birn & Priest, 2007), so the Sweet-Parker scaling would predict flares occur on timescales over four orders of magnitude longer than the tens of seconds to a few minutes that flares usually last. The magnetic diffusion model, scaling as $t_d \sim S_L t_A$ (see equation 1.8), fares even worse.

A number of alternative collisional reconnection models have been proposed to hasten the reconnection rate to values more consistent with flare observations, most famously the Petschek model (Petschek, 1964a) which assumes a shorter current sheet length L and thus modifies the surrounding magnetic field into an x-point topology with bent inflowing magnetic fields that produce standing slow-mode shocks, which do the majority of the work of heating and accelerating plasma. The bent magnetic field geometry of the Petschek model creates a wider exhaust region

at the sides of the current sheet, and thus reduces the bottleneck from mass conservation. This feature enhances the reconnection rate and thus improves on the timescale ($\sim \log(S_L)$), but relies on a number of conditions rarely met in naturally occurring reconnection (Birn & Priest, 2007), most notably requiring a spatially non-uniform (anomalous) resistivity highly enhanced at the x-line in order to remain self-sustaining, without which the current sheet evolves into an extended Sweet-Parker-type layer with the slower reconnection rate (Biskamp, 1986).

We note that the scaling equations 1.11, 1.13 and 1.17 from Sweet-Parker analysis are independent of resistivity. These results are agnostic to the mechanism that breaks the frozen-in condition in the current sheet, and thus are still useful in collisionless reconnection so long as it occurs in a steady-state and the upstream and downstream regions away from the current layer remain in the ideal MHD regime. The Petschek model also remains valuable beyond collisional reconnection, as its features such as the wider exhaust region and faster reconnection rates appear in collisionless reconnection, as we will see in the next section.

1.2.3 The Two-Fluid MHD Model and Collisionless Reconnection

Fortunately, there are alternative descriptions of magnetic reconnection that are suitable for systems with high Lundquist numbers (like many space plasmas) that do not require collisional resistivity or invoking the strict requirements of the Petschek model to produce reconnection rates that are more consistent with observation. One such model builds upon the fluid description, but instead of approximating

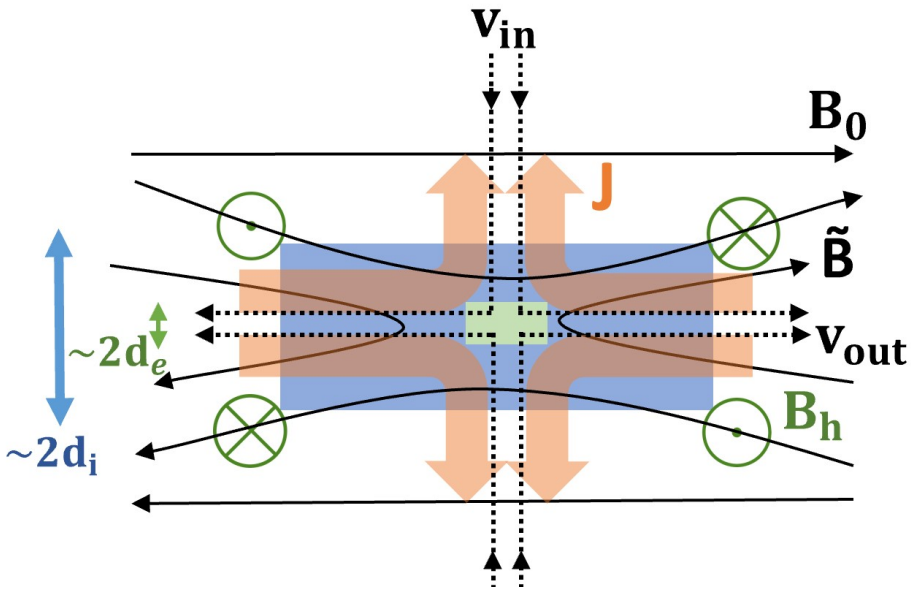

Figure 1.6 Sketch of anti-parallel Hall reconnection geometry in two-fluid MHD, showing the individual diffusion regions for ions (blue rectangle) and electrons (green rectangle) and a wider opening angle for the exhaust region than in Sweet-Parker geometry (Figure 1.5). The in-plane Hall current density J (orange arrows) is due to the electron fluid streaming past the demagnetized ions in the ion diffusion region, which produces the out-of-plane Hall magnetic field B_h (in green).

the plasma as a single fluid in which ions carry most of the momentum as in ideal and resistive-MHD, treats ions and electrons independently, obeying independent sets of fluid equations thus being called the "two-fluid model". Unlike in our earlier presentation of resistive-MHD, we are now interested in keeping the terms that are significant at the length scales of the gyro-orbits of electrons and ions that allow for the breaking of the frozen-in condition at small scales independently of resistivity. This hints at the possibility of obtaining reconnection rates that are independent of Lundquist number. The gyro-scale effects appear as corrections to the resistive Ohm's law (equation 1.6), which in the two-fluid model is now the generalized Ohm's law:

$$\mathbf{E} = -\frac{\mathbf{v} \times \mathbf{B}}{c} + \eta \mathbf{J} + \frac{\mathbf{J} \times \mathbf{B}}{nec} - \frac{\nabla \cdot \mathbf{P_e}}{ne} + \frac{m_e}{e^2} \frac{d\mathbf{J}/n}{dt}, \tag{1.19}$$

where the first two terms on the RHS are the usual convection and resistive terms from resistive MHD, followed by the Hall electric field, the divergence of the electron pressure tensor (more general than the scalar isotropic pressure we assumed in Sec. 1.2.1) and finally the electron inertia term. This form of Ohm's law comes from solving for the electric field in the electron momentum equation (not shown here), where we make the approximation $\mathbf{v_e} \approx -\mathbf{J}/ne$ for the electron velocity only in the electron inertia term, since the electrons move much faster than ions below ion gyro-scales and thus carry the majority of the net current. Thus, the two-fluid model captures physics at ideal MHD and electron and ion gyro-scales. For anti-parallel reconnection, the gyro-scales are the ion inertial length $d_i = c_A/\Omega_{ci}$, which is the Larmor radius for ions with velocity equal to the Alfvén speed and gyro-frequency $\Omega_{ci} = eB/m_i c$ and, analogously for electrons, the electron inertial length, $d_e = c_{Ae}/\Omega_{ce}$. The inertial lengths are also often expressed in terms of the plasma frequencies $\omega_{p\alpha} = \sqrt{4\pi n e^2/m_\alpha}$ as $c/\omega_{p\alpha}$, where α denotes either ions or electrons. The Hall term becomes significant at ion length scales, while the electron inertia and the off-diagonal electron pressure tensor terms are important are important at the much smaller electron scales.

With the inclusion of Hall and electron inertia physics, this model of non-ideal MHD is often called the "two-fluid model", but when electron inertia effects are absent the model is simply called Hall-MHD, where either the non-scalar part of the electron pressure or resistive terms, or in fact any other dissipation mechanism such as numerical diffusion in finite-difference computer simulations acting as an effective resistivity, can take the role of breaking the frozen-in condition and enable magnetic

reconnection. Curiously, numerical studies of steady-state collisionless reconnection have routinely shown that the normalized reconnection rate is $E' \sim 0.1$ independent of the system size or dissipation mechanism used (Shay et al., 1999a; Hesse et al., 1999; Birn et al., 2001), and experimental studies of collisionless reconnection have also shown rates exceeding the Sweet-Parker prediction (Ren et al., 2005; Cothran et al., 2005).

A sketch of steady-state 2D collisionless anti-parallel reconnection in the two-fluid model is shown in Figure 1.6, analogous to Figure 1.5 for Sweet-Parker reconnection, but with the inflowing and outflowing plasma (v_{in}, v_{out}) shown now as dotted lines and the reconnecting and reconnected magnetic fields ($B_0, \tilde{B}$) as solid black lines. The demagnetization of ions occurs at ion inertial scales $\sim d_i$, creating the ion diffusion layer shown as a blue rectangle, along with the the embedded electron diffusion layer shown as a green rectangle, emerging at scales $\sim d_e = \sqrt{m_e/m_i}d_i$. When the plasma is dragged in from upstream, the ions are demagnetized first, while the electrons continue their trajectory into the electron diffusion layer while still frozen-in to the now bent magnetic field. The electron motion produces the Hall electric current J shown as orange arrows, which due to Ampere's law, produce an out of plane magnetic field B_h shown in green that has a quadrupolar structure, a signature of Hall reconnection. An important difference with the Sweet-Parker reconnection geometry shown in Figure 1.5 is the much shorter horizontal extent of the dissipation region, which results in wider bent field lines at the exhaust region that allow for increased mass outflow, enhancing the reconnection rate.

Hall reconnection has been shown to be insensitive to the mechanism that

breaks the frozen-in condition in the Geospace Environmental Modeling (GEM) Magnetic Reconnection Challenge (Birn et al., 2001), a study that compared computational fluid, kinetic, and hybrid models to identify the minimum physics required to model collisionless reconnection. The Hall term in equation 1.19 was found to play a crucial role in widening the exhaust region and thus dramatically increasing reconnection rates beyond the Sweet-Parker model prediction. The wider exhaust region is often attributed to the introduction of dispersive waves at ion inertial scales (Mandt et al., 1994; Rogers et al., 2001). To motivate this, we recall that the Sweet-Parker model introduces the Alfvén wave which has a constant phase velocity $v_{ph} = c_A$ that is independent of wavenumber k (thus not dispersive) into reconnection due to the relaxation of the bent newly reconnected magnetic field lines emerging from the current layer (see Figure 1.5). In the Sweet-Parker model, the shape of the bent reconnected field line can be thought of as one quarter-wavelength of a standing Alfvén wave based on the upstream field, with a wavenumber $k \sim \pi/\delta$ (Drake et al., 2006), where δ is the full thickness of the Sweet-Parker layer. When the current layer thickness is on the order of ion gyro-scales however, ideal MHD no longer holds, so the Alfvén wave is replaced by smaller scale Hall MHD waves. These are the whistler wave with $v_{ph} = kc_A d_i$ and in the presence of a large out-of-plane (guide) magnetic field (see Sec. 1.2.4), the kinetic Alfvén wave with $v_{ph} = kc_A\rho_s$, where ρ_s is the ion sound Larmor radius. For thin current sheets (with thicknesses such that $kd_i > 1$, or $k\rho_s > 1$ in the strong guide field limit), the bent field lines create super-Alfvénic reconnection outflows close to the x-line where Hall MHD holds, which then then run into the further downstream Alfvénic flow where ideal

MHD dominates, forcing a vertical displacement of the newly frozen-in reconnected field lines to maintain continuity and widening the exhaust region, enabling fast reconnection.

The dispersive wave model is just one mechanism suggested to cause fast reconnection, and it has been shown that reconnection remains fast even in systems without dispersive waves. For example, numerical work on electron-positron plasmas still show fast reconnection rates in the absence of whistler or kinetic Alfvén waves (since in an electron-positron plasma, $d_i/d_e = \sqrt{m_i/m_e} = 1$, so the Hall current vanishes), and this has instead been attributed to non-diagonal electron pressure tensor terms acting as an effective spatially localized resistivity analogous to the anomalous resistivity invoked to sustain the wider exhaust field geometry in the Petschek model (Bessho & Bhattacharjee, 2005; Daughton & Karimabadi, 2007; Chacón et al., 2008). Additionally, the suppression of dispersive waves in kinetic simulations of Hall reconnection using extremely large out-of-plane (guide) magnetic fields (Liu et al., 2014) have also shown fast reconnection rates are achievable, which the authors claim potentially challenges the present understanding of the role of dispersive waves in fast reconnection. However, a definitive demonstration that slow reconnection takes place in the presence of dispersive waves is needed to confirm what is suggested by these works.

Very recently, theoretical work has determined a first-principles theory explaining the open exhaust geometry and the observed "0.1" scaling of the collisionless reconnection rate (Liu et al., 2022). This model attributes the open exhaust geometry to the fact that within the ion diffusion region where the Hall term dominates,

the divergence of the Poynting vector is $\nabla \cdot \mathbf{S} \approx -\mathbf{J} \cdot (\mathbf{J} \times \mathbf{B}/nec) = 0$, meaning the Hall electric field does not do work on the plasma and directs energy away from the ion diffusion region, creating a spatially localized energy void at the x-line. The resulting energy void - or equivalently pressure depletion - at the x-line forces the upstream magnetic field to bend inward sharply towards the x-line to achieve force balance, therefore widening the exhaust region. The "0.1" scaling was then demonstrated to arise from force balances between electron, ion and MHD scales and the assumptions of the model were validated with 2D particle-in-cell (PIC) simulations. This is contrasted with Sweet-Parker reconnection, where $\nabla \cdot \mathbf{S} = -\mathbf{J} \cdot (\eta \mathbf{J}) = -\eta J_z^2$ (where J_z is the out-of-plane current in the sheet) which distributes energy all along the extended length of the current layer, thus not creating a localized pressure depletion at the x-line that favors a wide exhaust geometry, explaining the slower reconnection rate. This model also explains why electron-positron reconnection is fast in the complete absence of the Hall current, due to a similar highly localized pressure depletion zone forming at the x-line.

1.2.4 Component or Guide Field Reconnection

Up to this point, the models discussed all have assumed completely anti-parallel reconnecting magnetic fields, but in naturally occurring reconnection, this is not always the case. For example, the polarity of the IMF colliding with Earth's dayside magnetosphere is highly variable on the scale of minutes and does not always have a southward orientation such as in Figure 1.4. Dayside magnetopause

reconnection is sketched in Figure 1.7 as viewed from the Sun, with a south-east IMF orientation with $B_y > 0$ (upper drawing) and south-west IMF orientation with $B_y < 0$ (lower drawing), using Geocentric Solar Magnetospheric (GSM) coordinates where X_{GSM} is the Sun-Earth direction with the origin at Earth and Sun at $X_{GSM} > 0$, Y_{GSM} (simply Y in Fig. 1.7) is defined as the cross product of X_{GSM} with the Earth's dipole axis directed positive towards dusk and Z_{GSM} completes the right-handed coordinate system. The thin diagonal black arrows represent the IMF, shown reconnecting with the northward geomagnetic field (black ovals), with the thick arrows representing the magnetic tension force pulling apart the newly reconnected field lines. It is called "component reconnection" when an out-of-plane component of the magnetic field - called the guide field - is present during reconnection. Guide field reconnection is common in the solar corona, solar wind, dayside magnetopause, and toroidal fusion devices, but not in the magnetotail where guide field is typically weak.

We find that understanding three-dimensional spreading of guide field reconnection, which will be discussed in Sec. 1.3 and Sec. 2.4, relies on the physics of two-dimensional guide field reconnection, so here we briefly summarize the basic changes to two-dimensional reconnection for the case of a uniform guide field. A qualitative understanding of what a guide field does for Hall reconnection can be gained from Figure 1.8, which shows a sketch of the reconnecting plane in steady-state component Hall reconnection analogous to Figure 1.6 but with a uniform guide field B_g (in light blue) permeating everywhere. The guide field modifies the two-fluid structure of the reconnecting layer, changing the effective range of the Hall electric field from

the ion inertial scale d_i to the ion sound Larmor radius $\rho_s = c_s/\omega_{ci} = \sqrt{\beta/2}d_i$, where $\beta = P/P_m$ is the ratio of the plasma pressure P to the magnetic pressure P_m, $c_s = \sqrt{(\gamma_e Z k_B T_e + \gamma_i k_B T_i)/m_i}$ is the ion sound speed, γ_e and γ_i are the ratios of specific heats for electrons and ions, Z is the effective charge on the ion (greater than unity for multiple ionization states), k_B is Boltzmann's constant, and T_i and T_e are the ion and electron temperatures, respectively. The presence of a guide field also introduces the electron thermal Larmor radius $\rho_e = v_{th,e}/\omega_{ce}$, where $v_{th,e} = \sqrt{k_B T_e/m_e}$ is the electron thermal speed.

The guide field combines with the out-of-plane quadrupolar Hall magnetic field B_h (in green), resulting in the breaking of the symmetry of the magnetic pressure profile P_m across the ion diffusion region (blue rectangle).Where the guide field is parallel to the Hall magnetic field, the magnetic pressure is enhanced, and is reduced where they are anti-parallel. This creates opposing magnetic pressure gradients $-\nabla P_m$ across each side of the ion diffusion region shown as purple arrows. In order to maintain a steady-state, counteracting fluid pressure gradients $-\nabla P$ arise, shown as red arrows, creating a quadrupolar structure in the fluid pressure that does not appear in anti-parallel Hall reconnection. The fluid pressure gradients cause ions to drift across the magnetic field at the exhaust region, creating voids and enhancements of the ion density where the total magnetic pressure is highest and lowest, respectively, indicated by the labels n_{low} and n_{high}, and electrons accelerate along the magnetic field to short out the resulting electric field, preserving quasi-neutrality. The quadrupole in the density that accompanies the quadrupole in the fluid pressure is a characteristic signature of component Hall reconnection (Kleva

et al., 1995; Pritchett & Coroniti, 2004; Drake et al., 2005). Another qualitative aspect of component Hall reconnection is that the exhaust region takes on a rotated or tilted appearance (not shown), caused by the same cross-field ion drifts and electron motion.

1.2.5 Embedded Reconnection

Embedded reconnection (Shay et al., 2004) arises when reconnection starts in a current sheet with a half-thickness that is larger than the ion inertial scale $\delta > d_i$ (for anti-parallel fields, but embedded reconnection can also occur with a guide field). In this scenario, the reconnection rate is initially slow, due to the fact the upstream magnetic field B_{up} at the edges of the ion diffusion region is lower than the asymptotic magnetic field B_0 far upstream at a distance δ from the x-line. Assuming the upstream magnetic field varies linearly along the inflow direction y with the origin at the x-line, at the upstream edge of the IDR the reconnecting magnetic field scales as $B_{up} \sim (d_i/\delta)B_0$ (Shay et al., 2004). As reconnection progresses, the inflow carries a stronger magnetic field into the diffusion region, which gradually reduces the width of the current sheet. When the current sheet collapses down to ion inertial scales $\delta \sim d_i$, reconnection reaches a quasi-steady-state with the characteristic fast rate, as the full strength of the upstream magnetic field B_0 flows into the diffusion region.

Reconnection initiates in many real systems in a qualitatively similar way: with current sheets much wider than ion inertial scale. For example, in magnetotail

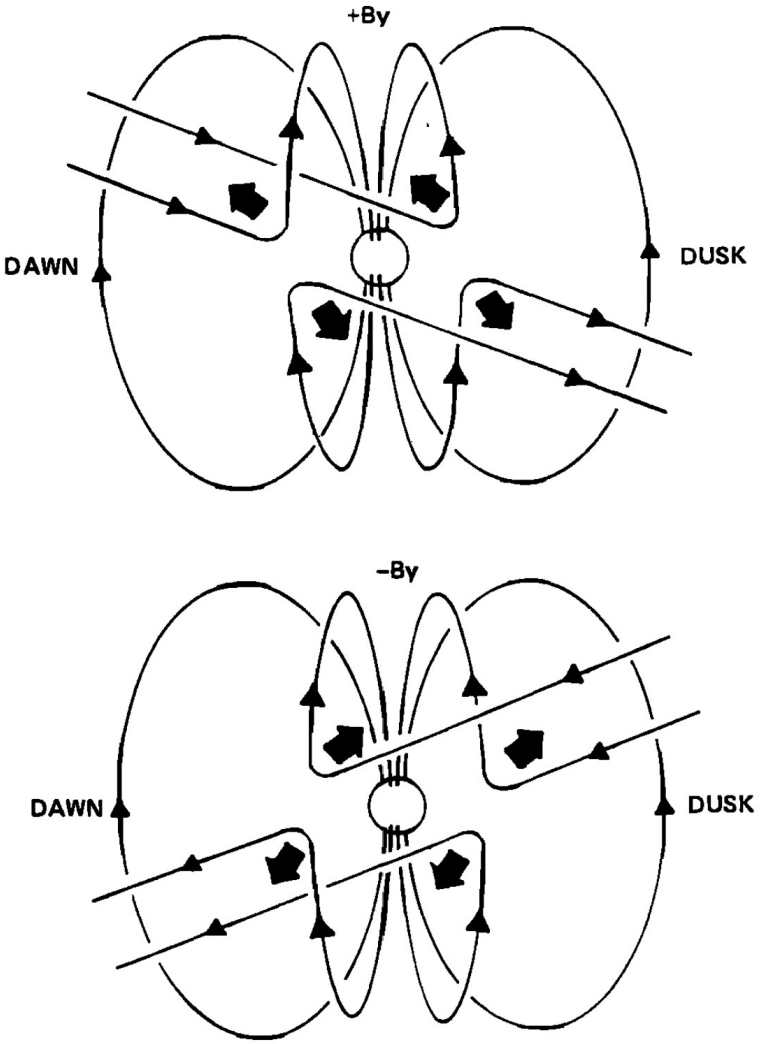

Figure 1.7 Schematic drawings of reconnection at the dayside magnetopause as viewed from the Sun. The large arrows indicate the direction of the forces associated with magnetic tension on recently reconnected field lines. When the y component of the interplanetary magnetic field is positive (upper drawing), these forces pull the recently reconnected field lines toward the dawnside of the northern polar cap and the duskside of the southern polar cap as the field lines are dragged tailward by the flow of the solar wind. Similarly, when the interplanetary magnetic field is negative (lower drawing), the reconnected field lines are pulled toward the duskside of the northern polar cap and the dawnside of the southern polar cap. Such effects are believed to be the origin of asymmetric polar cap convection and related phenomena. Original figure and caption reproduced with permission from Gosling et al. (1990).

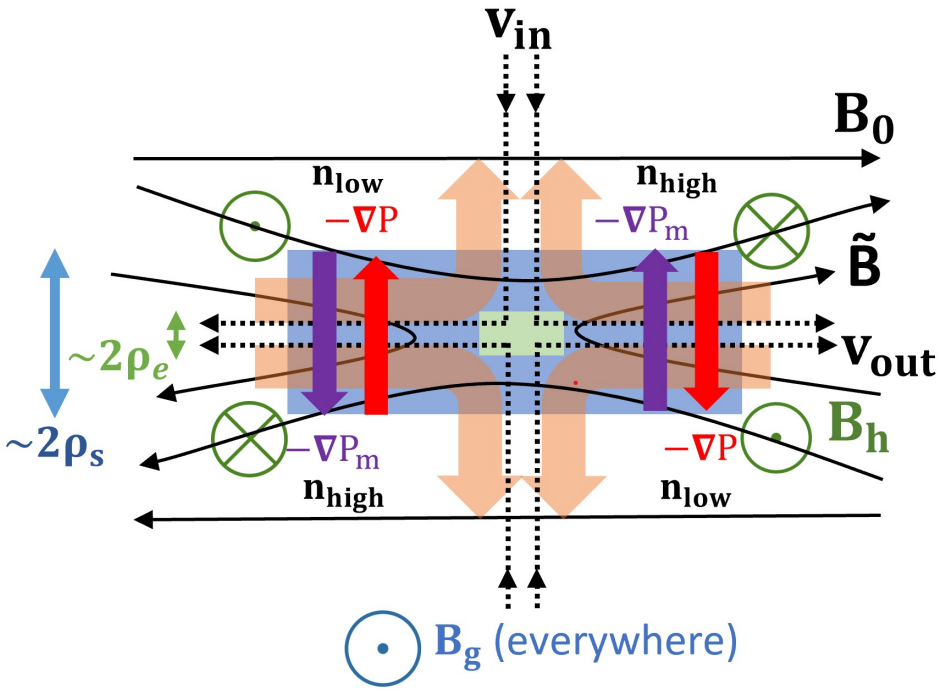

Figure 1.8 Sketch of component Hall reconnection geometry in two-fluid MHD, analogous to Figure 1.6 but with an out-of-plane guide magnetic field B_g (in blue) introducing cross-field ion drifts (red arrows) at the left and right edges of the ion diffusion region. See text for the definition of the symbols.

reconnection, the magnetotail current sheet is known to have thickness at midnight of roughly $\sim 30d_i$ during quiet times and thins down to $\sim 1d_i$ at the start of a substorm (Sergeev et al., 1990). In the solar corona, though current sheet thicknesses are not resolvable, the ion inertial scale for the quiet Sun is on the order of $d_i \sim 1$, significantly smaller than the dimensions of a flux rope, so it is reasonable to expect reconnection in the corona to be embedded in current sheets wider than d_i.

1.3 3D Spreading of Magnetic Reconnection

Early models treated reconnection as two-dimensional (2D) (Sweet, 1958; Parker, 1957; Petschek, 1964b), but naturally-occurring reconnection is a 3D process [*e.g.*, (Pontin, 2011; Lukin & Linton, 2011)]. One aspect of the 3D nature of reconnection is that the x-line where the magnetic field topology changes has a finite extent in the direction normal to the plane of reconnection. Spatially confined reconnection in which the extent of the reconnecting x-line does not change in time has been studied theoretically and numerically (Shay et al., 2003; Linton & Longcope, 2006; Meyer III, 2013; Sasunov et al., 2015; Shepherd et al., 2017; Liu et al., 2019; Huang et al., 2020; Pyakurel et al., 2021). Spatially confined x-lines can be fixed in space or convect without the region undergoing reconnection elongating in the out of plane direction (Shay et al., 2003).

An important manifestation of the 3D nature of naturally occurring reconnection is that the reconnecting x-line can elongate in the out of plane direction over time, which we synonymously call spreading. Figure 1.9 shows a sketch of anti-

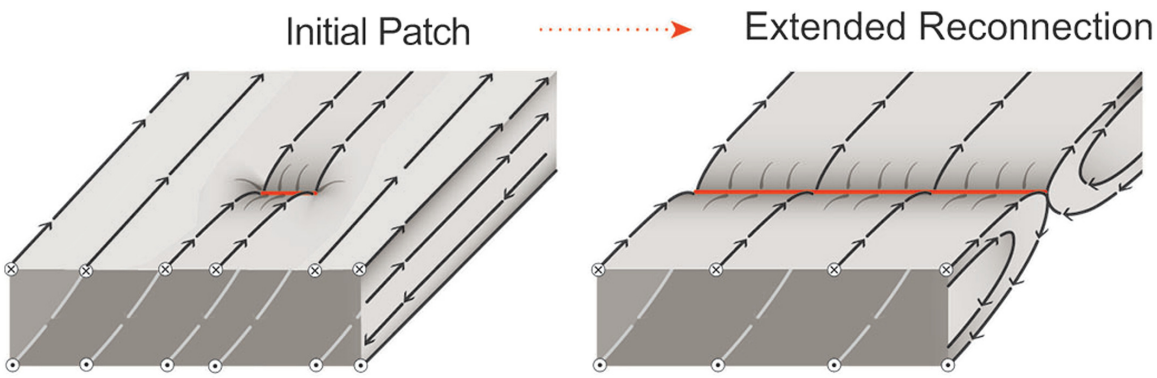

Figure 1.9 Schematic diagram of reconnection spreading. Initiation occurs in a spatially localized region (left) and spreads into an extended line (right). The region of reconnection is shown in red. Original figure and caption reproduced with permission from Walsh et al. (2018) under the terms of the Creative Commons Attribution-Non-Commercial-NoDerivs License.

parallel quasi-2D reconnection (meaning initially spatially invariant in the out of plane direction, in contrast to fundamentally 3D reconnection which does not have any symmetry direction in the initial condition) with the reconnecting x-line in red spreading in the out of plane direction, extending the reconnection region. Such behavior has been inferred from the elongation of chromospheric ribbons during two-ribbon solar flares such as in Figure 1.3 (Isobe et al., 2002; Lee & Gary, 2008; Qiu, 2009; Qiu et al., 2010; Liu et al., 2010; Cheng et al., 2011; Tian et al., 2015; Graham & Cauzzi, 2015; Qiu et al., 2017) and eruptions of solar prominences (large loop-like structures protruding from the photosphere into the corona that are typically long lived before undergoing an abrupt eruption and cooler than the coronal plasma) (Tripathi et al., 2006), and directly observed at Earth's magnetopause (Zhou et al., 2017; Zou et al., 2018; Zou et al., 2019), in Earth's magnetotail (McPherron et al., 1973; Nagai, 1982; Nagai et al., 2013; Hietala et al., 2014), and in laboratory reconnection experiments (Katz et al., 2010; Egedal et al., 2011; Dorfman et al., 2013,

2014), and is thought to result in the production of x-lines as long as 400 Earth radii in the solar wind (Phan et al., 2006; Gosling et al., 2007; Shepherd et al., 2017). Studying how reconnection spreads, which is the focus of the present study, is important in many settings because it impacts secondary processes such as particle acceleration and the global efficiency of the release of large-scale magnetic energy.

There have been many numerical studies of 3D reconnection spreading in various settings. During anti-parallel quasi-2D reconnection, the consensus is that spreading occurs in the direction perpendicular to the reconnection plane at the speed and direction of the current carriers (Huba & Rudakov, 2002, 2003; Shay et al., 2003; Karimabadi et al., 2004; Lapenta et al., 2006; Shepherd & Cassak, 2012; Nakamura et al., 2012; Meyer III, 2013; Jain et al., 2013; Jain & Büchner, 2017; Arencibia et al., 2021). If one species carries all the current, the spreading is unidirectional; if both species carry some current the spreading is bidirectional. While the ions carry most of the current in the quiet plasma sheet, the electrons carry the current when the plasma sheet thins down when reconnection takes place (Jain et al., 2021), so the direction of the spreading is consistent with the direction of the current carriers. This directionality of the spreading is consistent with observations of reconnection during geomagnetic substorms, which spread in the dawnward direction (*i.e.*, in Fig. 1.4 the x-line in the magnetotail spreads into the page) (McPherron et al., 1973; Nagai, 1982; Nagai et al., 2013).

A number of physical mechanisms for spreading have been suggested. It was argued (Huba & Rudakov, 2002) that spreading of collisionless reconnection is caused by electrons convecting the reconnected magnetic into the region not undergoing

reconnection [see also (Hesse et al., 2001; Shay et al., 2003)]. They argued it was caused by a shock-like "reconnection wave" due to the Hall effect and motivated the result using linear theory. Assuming the Hall electric field in equation 1.19 dominates within the ion diffusion layer, the induction equation 1.4 becomes the electron magnetohydrodynamic (eMHD) induction equation

$$\frac{\partial \mathbf{B}}{\partial t} = \frac{1}{ne}\nabla \times (\mathbf{J} \times \mathbf{B}). \tag{1.20}$$

Linearizing around the out of plane current profile, the perturbed reconnected (normal) magnetic field B_{1n} is governed by

$$\frac{\partial B_{1n}}{\partial t} + \frac{\mathbf{J}}{ne} \cdot \nabla B_{1n} = 0. \tag{1.21}$$

This shows that the magnetic field of the x-line is convected at a velocity associated with the current carriers, assumed to be electrons in their work. When ions carry some of the current, spreading occurs at the speed of the current carriers in their respective directions (Shay et al., 2003; Lapenta et al., 2006; Nakamura et al., 2012). If the half-thickness of the current sheet is w_0, then in the reference frame in which the electrons carry all the current, the spreading speed v_s scales as (Shay et al., 2003)

$$v_s \sim \frac{J}{ne} \sim \frac{cB_0}{4\pi new_0} = c_A \frac{d_i}{w_0}. \tag{1.22}$$

The functional dependence on w_0 was confirmed in simulations (Shay et al., 2003), and it was similarly shown that the relevant speed of the current carriers is that

of the initial current sheet half-thickness w_0 rather than the kinetic-scale thickness after reconnection has started (Lapenta et al., 2006; Li et al., 2020). Interestingly, it was shown that reconnection does not spread in the resistive-MHD model if electrons carry all the current for anti-parallel reconnection (Nakamura et al., 2012).

An alternate mechanism for collisionless anti-parallel reconnection spreading was presented, based on pressure instead of magnetic field (Huba & Rudakov, 2003; Nakamura et al., 2012). The region where reconnection occurs was found to be of lower plasma pressure than the non-reconnecting regions. The low pressure convects with the current carriers into the non-reconnecting regions, inducing inwards flow which causes reconnection sequentially in the out of plane direction. A related model was developed to explain observations of impulsive reconnection in the Magnetic Reconnection eXperiment (MRX) (Dorfman et al., 2013, 2014). In their experiment, the initial conditions had an electron flow gradient in the out of plane direction. The diverging flow requires an inflow in an adjacent non-reconnecting region to preserve mass continuity, producing a sequential onset of reconnection.

Another model of spreading, developed to explain observations of the sequential brightening X-ray flare loops in solar flares, suggested a propagating ideal MHD wave triggers instabilities in pre-flare coronal magnetic field structures, causing reconnection to occur over an extended region (Vorpahl, 1976). This work suggests that reconnection spreading is mediated specifically by the perpendicularly-propagating fast magnetosonic wave, which has a phase velocity consisting of the sound and Alfvén speeds added in quadrature $v_{ph} = \sqrt{c_s^2 + c_A^2}$ and describes a wave propagating perpendicular to the magnetic field driven by compression and

rarefaction of the plasma density (like a conventional sound wave) coupled with simultaneous enhancements and reductions of the magnetic pressure where the density is higher and lower, respectively. This hypothesis is tested with a numerical experiment (Arencibia et al., 2021), which is detailed in Sec. 5.5.

Spreading of magnetic reconnection is qualitatively different when there is a background out of plane (guide) magnetic field, which commonly is present in reconnection in solar flares (Qiu et al., 2017), the solar wind (Gosling et al., 2005), and the dayside magnetopause (Zou et al., 2018). Laboratory experiments showed that, for a strong guide field, the spreading is bidirectional with a speed given by the Alfvén speed $c_{Az} = B_{0z}/(4\pi m_i n)^{1/2}$ based on the guide field strength B_{0z} rather than the speed of the current carriers (Katz et al., 2010):

$$v_s = \pm c_{Az}. \tag{1.23}$$

Two-fluid MHD simulations found the same scaling with the out-of-plane (guide) magnetic field (Shepherd & Cassak, 2012; Jain & Büchner, 2017). The spreading has been described as being mediated by Alfvén waves (Shepherd & Cassak, 2012), whistler waves and flow induced waves (Jain & Büchner, 2017), and kinetic Alfvén waves (Li et al., 2020). Recently, it was shown in simulations of guide field reconnection with asymmetric plasma conditions that spreading in current sheets thinner than ion scales is bidirectional at the Alfvén speed, but is at the current carrier speed for thicker current sheets (Li et al., 2020). The different behavior for different current sheet thicknesses was attributed to the reduced tearing instability growth

rate for wider current sheets.

Observations of ribbon spreading in two-ribbon solar flares (Qiu et al., 2017) and dayside magnetopause x-line spreading (Zou et al., 2018) often show spreading happening slower than the predicted speeds in Eqs. 1.22 for anti-parallel reconnection and 1.23 for guide field reconnection, and it is not currently understood why this is the case. Using the results developed in this dissertation, we offer potential explanations for this behavior in Chapter 6.

1.4 Reconnection Spreading in Non-Uniform Current Sheets

Most of the previous theoretical and numerical work on the spreading of reconnection has addressed quasi-2D anti-parallel reconnection in uniform current sheets with an initial half-thickness $w_0 \sim d_i$. However, reconnecting current sheets in naturally occurring physical systems such as the solar corona and the dayside magnetopause and magnetotail of Earth and other planets are unlikely to have a thickness that is uniform in the out-of-plane direction before reconnection onsets and spreads. For example, *in situ* observations of the near-Earth magnetotail plasma sheet during quiet times show the half-thickness varies continuously in the dawn-dusk direction from a minimum of $< 3\ R_E$ (Earth radii) at midnight in magnetic local time up to $\sim 8\ R_E$ at the flanks, and thins down to $\sim 0.1-0.4\ R_E$ at midnight and $\sim 1\ R_E$ at the flanks at the end of a substorm growth phase, prior to fast reconnection onset (Fairfield, 1979, 1980; Voigt, 1984; Sergeev et al., 1990; Kaymaz et al., 1994; Tsyganenko, 1998), where R_E denotes the radius of Earth. Figure 1.10

shows multiple cross-sections of the near-Earth magnetotail current sheet in the $Y_{GSM}Z_{GSM}$ plane, where the tick marks are distances of $2R_E$. The cross sections at distances $-15, -30$ and $-60R_E$ from Earth (in descending order) show a parabola-like profile of the current sheet thickness in the dawn-dusk direction that is thinnest at midnight and widest at the dawn and dusk flanks.

While there has been a numerical study of a current sheet of non-uniform thickness that was extremely thick outside the reconnection region so that the x-line remained spatially confined (Huang et al., 2020), we are unaware of any studies that predict the spreading speed of reconnection in current sheets of a non-uniform thickness.

1.5 Summary of Dissertation Research

This dissertation contains a number of new results on the fundamental physics of the spreading of reconnection of finite extent (Arencibia et al., 2021, 2022). We generalize the theory of anti-parallel reconnection spreading (Huba & Rudakov, 2002), showing that it can be interpreted in the form of a scaling analysis and showing that the same theory can be used to derive from first-principles the scaling of the spreading speed in the strong guide field limit, thereby uniting the understanding of reconnection spreading under a single first-principles approach. We also extend the new theoretical model to systems with current sheets with thicknesses that vary in the out-of-plane direction and discuss the implications. New results include: (1) We argue that the key physical aspect of x-line spreading is the induction of an

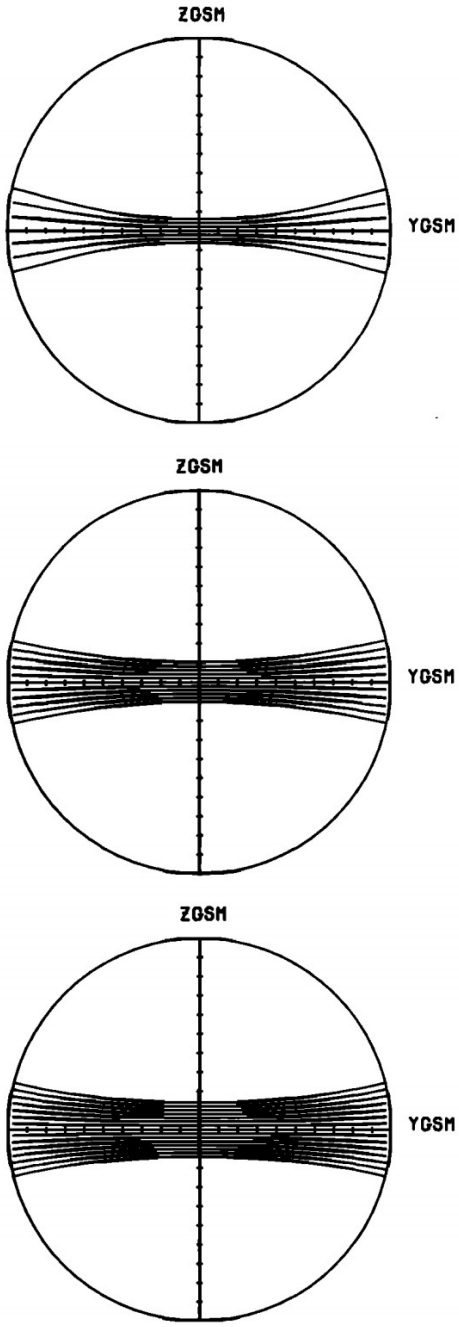

Figure 1.10 Tail cross sections showing the computed tail current streamlines that form the tail plasma sheet. Tail radius is $R = 20R_E$, dipole tilt angle is $\Psi = 0°$. From top to bottom, tail cross sections are taken at $X_{GSM} = -15R_E, -30R_E$, and $-60R_E$. The plasma sheet thickness increases in the Y_{GSM} direction toward the flanks of the tail. Note also that the tail plasma sheet becomes thicker and more diffuse with increasing distance from Earth. Original figure and caption reproduced with permission from Voigt (1984).

x-line topology in the non-reconnecting region [see also Jain et al. (2013)], which is carried out by the gradient in the electric field in the outflow direction at the interface between the reconnecting and non-reconnecting regions. If an x-line topology is not induced in a given direction, reconnection does not spread in that direction. (2) The physical cause of reconnection spreading without and with a guide field are different, with convection at the Hall scale and MHD-scale magnetic field bending, respectively, playing key roles. We validate the theoretical results using 3D two-fluid and resistive-MHD numerical simulations, for both anti-parallel and guide field reconnection. (3) The theory explains why anti-parallel reconnection in the resistive-MHD model does not spread (Nakamura et al., 2012). (4) We find that a determining factor for whether a current sheet spreads or convects with a fixed length in a numerical simulation is the aspect ratio of the domain, which we suggest is controlled by the amount of free magnetic energy in the system. (5) We perform a test of whether the results obtained herein are dependent on the manner in which reconnection is excited in the system and use the result to test whether the excitation of fast magnetosonic waves in the out of plane direction cause reconnection to spread, as had previously been suggested (Vorpahl, 1976). Physically, this mechanism could occur if reconnection is initiated through a pressure pulse squeezing the current sheet. As simulations typically initiate reconnection using a magnetic perturbation, it is important to assess whether the speed of the spreading depends on the way in which reconnection is seeded. Using a pressure pulse to initiate reconnection, we find that anti-parallel reconnection spreads at the current carrier speed rather than the magnetosonic speed. (6) Finally, we present a first-principles

scaling theory of the spreading of collisionless anti-parallel reconnection in current sheets of non-uniform thickness. We include predictions for spreading from a thinner to thicker current sheet and for spreading from a thicker to a thinner current sheet. Physically, one might expect reconnection in a current sheet of non-uniform thickness to spread from a thin region to a thick region, but observations of Earth's magnetotail (Nagai et al., 2013) suggest that spreading from a thick region to a thin region can also occur. For reconnection that spreads from a thinner into a thicker part of a current sheet, a key result is that the spreading speed in the thicker region is slower than the spreading speed based on current knowledge for a uniform sheet of equivalent local thickness, due to a reduction in the initial effective reconnecting field via embedding (Shay et al., 2004). This provides a mechanism for reconnection spreading that is sub-Alfvénic as well as slower than the local current carriers in the macroscopic current sheet. This result is important because observations of dayside reconnection (Zou et al., 2018) and two-ribbon solar flares (Qiu et al., 2017) suggest that the spreading speed is slower than expected from the existing theory. We confirm our prediction with a suite of 3D two-fluid numerical simulations. We use our prediction for the spreading speed to calculate the time it takes reconnection to spread a particular distance. We apply our results to reconnection in Earth's magnetotail, and motivate potential observational signatures of spreading in current sheets of non-uniform thickness in solar flares.

The layout of this dissertation is as follows. In Chapter 2, we discuss the theory of 3D reconnection spreading and derive a number of key implications about the physical cause of reconnection spreading and applications to collisionless and

collisional systems with and without a guide field. In Chapter 3, we present a theory of 3D reconnection spreading in current sheets of non-uniform thickness. In Chapter 4, we discuss the setup of our numerical simulations. In Chapter 5, we discuss the results of our simulations and validate the theoretical models. In Chapter 6, we apply our model from Chapter 3 to reconnection spreading in the near-Earth magnetotail and solar flares, and offer conclusions in Chapter 7.

Chapter 2

Theory of Reconnection Spreading in Current Sheets of Uniform Thickness

2.1 General Considerations

We use a coordinate system in which z is the direction of the initial current, the current sheet is centered around $y = y_{cs}$, and x is the direction of the equilibrium reconnecting magnetic field, with $B_x > 0$ for $y < y_{cs}$ and $B_x < 0$ for $y > y_{cs}$. We use a reference frame where the electrons fully carry the out of plane current. The asymptotic reconnecting magnetic field strength is B_0, there may be a guide field of strength B_{0z}, and the current sheet has an initial half-thickness w_0. The system is sketched schematically in Fig. 2.1 for the case without a guide field. The $y = y_{cs}$ plane is shown with two dotted lines. At a given time, reconnection is occurring in a localized part of the current sheet with finite out of plane extent 2λ, shown with orange shading in the figure, while the parts of the system shaded blue are not undergoing reconnection.

As in the model reviewed in the Sec. 1.3, we consider the time evolution of the reconnected magnetic field B_y. To generalize the previous approach (Huba & Rudakov, 2002), we begin from Faraday's law, $\partial \mathbf{B}/\partial t = -c\nabla \times \mathbf{E}$, where $\mathbf{E}$ is the electric field. At the interface between reconnecting and non-reconnecting regions,

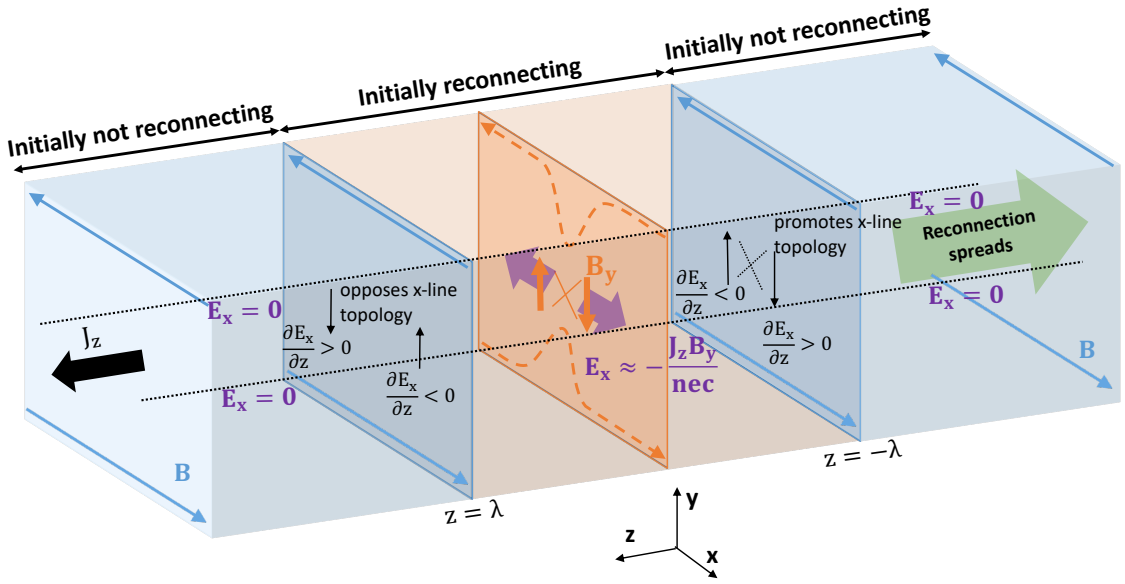

Figure 2.1 Sketch of a system undergoing anti-parallel reconnection in a localized region in the out of plane direction from $-\lambda < z < \lambda$, motivating the physics behind why reconnection spreads in the direction of electron convection. Orange shading denotes the finite domain where reconnection is taking place, and it is not taking place in the blue shaded region. The projection of a representative reconnecting magnetic field line in the orange region is shown in the xy plane as the dashed orange line, with an orange X denoting the x-line. The reconnected components of the magnetic field in the orange region are denoted by thick vertical orange arrows. The Hall electric field component E_x shown as purple arrows points away from the x-line in the reconnecting region and is zero elsewhere. The gradient in E_x at the $z = -\lambda$ interface produces a normal magnetic field B_y that promotes an x-line topology (black arrows), extending the x-line and causing spreading. At the $z = \lambda$ edge, the B_y produced opposes an x-line topology (black arrows), so reconnection does not spread in that direction.

gradients in the z direction exceed gradients in the x direction, so the term that dominates B_y production is [see also (Jain et al., 2013)]

$$\frac{\partial B_y}{\partial t} \approx -c\frac{\partial E_x}{\partial z}. \tag{2.1}$$

A scaling analysis allows us to find a characteristic out of plane spreading speed v_s, given by

$$v_s = \frac{\Delta z}{\Delta t} \approx -c\frac{\Delta E_x}{\Delta B_y}, \tag{2.2}$$

where the spatial finite difference Δz is evaluated at the boundary between the reconnecting and non-reconnecting regions, and we associate $\Delta z/\Delta t$ with the speed of the spreading v_s. We retain the minus sign, as it gives information about the direction of propagation.

We first make contact with previous work. For anti-parallel collisionless reconnection, it was argued that reconnection spreading occurs via out of plane convection by the electrons. The electric field associated with this is $E_x \sim -J_z B_y/nec$, from the Hall term. Using this in Eq. (2.2) and taking $\Delta B_y \simeq B_y$ at the interface between reconnecting and non-reconnecting regions gives

$$v_s \approx \frac{\Delta(J_z B_y/ne)}{\Delta B_y} \approx \frac{J_z}{ne}. \tag{2.3}$$

This reproduces the result that reconnection spreads at the speed and direction of the current carriers in Eq. (1.21). In our approach, the result follows from a scaling analysis rather than linear theory.

In what follows, we argue that Eq. (2.2) is useful for predicting the spreading speed beyond only anti-parallel reconnection. More generally, the component of the net electric field in the outflow direction E_x is given by the generalized Ohm's law

$$E_x = -\frac{v_y B_z - v_z B_y}{c} + \frac{J_y B_z - J_z B_y}{nec} - \frac{1}{ne}\frac{\partial p_e}{\partial x} + \frac{m_e}{ne^2}\frac{dJ_x}{dt} + \eta J_x, \qquad (2.4)$$

where $\mathbf{v}$ is the (ion) bulk flow velocity, p_e is the (scalar) electron pressure, m_e is the electron mass, and η is the resistivity. The right hand side includes the convection term, Hall term, electron pressure gradient term, electron inertia term, and resistive term in order of appearance. We show that in different settings, different terms can dominate. We find the electron pressure gradient and electron inertia terms do not impact spreading in current sheets at or above ion inertial scale thicknesses.

Before considering specific systems, we elucidate what our approach reveals about the physical mechanism for reconnection spreading. Previous work (Huba & Rudakov, 2002) suggested the evolution of B_y is what determines spreading. Physically, in order to seed an x-line in a plane in which there is initially no x-line, one needs to generate a normal magnetic field B_y with a bipolar structure of the proper polarity [see also (Jain et al., 2013)]. If the x coordinate of the x-line is x', then an x-line is seeded if $B_y > 0$ for $x < x'$ and $B_y < 0$ for $x > x'$ for the assumed B_x directionality. From Eq. (2.1), the signs of the gradient of the electric field E_x at the ends of the region undergoing reconnection determine whether $\partial B_y/\partial t$ is locally positive or negative for $x < x'$ and $x > x'$, which determines whether an x-line develops over time in the non-reconnecting region. We argue the sign

of the gradient of the electric field in the outflow direction is a more fundamental interpretation of how reconnection spreads via convection.

We note a subtlety that is important for numerical studies of reconnection spreading and may be important in naturally occurring reconnection. Many theoretical developments of reconnection spreading, including the treatment in this section, are based on the propagation of a small B_y into regions not previously undergoing reconnection. However, the presence of B_y is not synonymous with the onset of reconnection. Rather, the presence of B_y triggers the tearing instability (Furth et al., 1963) which makes B_y grow in time, and it is only after getting to large amplitudes that steady reconnection is set up. Thus, there is a time delay between when B_y spreads into a region not undergoing reconnection and when reconnection begins in earnest. This has been seen in previous simulation studies (Huba & Rudakov, 2002), and more recently has been noted as an important factor in the spreading of reconnection in thick current sheets for which the time scale of the tearing instability is longer (Li et al., 2020). For the present study, the time delay between the appearance of B_y and the onset of full-fledged reconnection is the same at all locations, so the spreading speed of reconnection is unchanged by the delay. Consequently, in this study, it is sufficient to study the spreading speed of the normal magnetic field B_y as a proxy for the spreading speed of the onset of full-fledged magnetic reconnection.

2.2 Spreading of Collisionless Anti-Parallel Reconnection

We exploit the results of the previous section to develop new insight on the physics of spreading for anti-parallel collisionless (Hall) reconnection. In Fig. 2.1, the dark blue arrows represent magnetic field lines within the blue shaded regions in which reconnection is not taking place, which are straight because there is no reconnection to bend them towards the $y = y_{cs}$ plane. In contrast, the dashed orange arrows depict the projection of a representative reconnecting magnetic field line in the xy plane within the orange shaded region where reconnection is occurring, which bend in towards the x-line. As previously noted (Huba & Rudakov, 2002; Shay et al., 2003), the out of plane current is carried in the z direction by electrons convecting in the $-z$ direction. Thus, the x-line topology governed by B_y, depicted by the thick vertical orange arrows in the region undergoing reconnection, is convected in the $-z$ direction and reconnection spreads in that direction (the green arrow) in this reference frame.

We reinterpret this in terms of the electric field E_x and the induced magnetic field in the non-reconnecting regions. In the region where reconnection is taking place, the out of plane current J_z (the thick black arrow) in the presence of the reconnected magnetic field B_y (the thick orange arrows, negative for $x > x'$, positive for $x < x'$) produces a non-zero component of the Hall electric field in the outflow direction $E_x \approx -J_z B_y/nec$, pointing away from the x-line as denoted by the purple arrows. This E_x is relatively uniform between $z = -\lambda$ and $z = \lambda$, but at the boundaries of the reconnecting region at $z = \pm\lambda$, there is a non-zero out of plane

gradient $\partial E_x/\partial z$. From Faraday's law, this produces a $\partial B_y/\partial t$ in the adjacent non-reconnecting planes, positive for $x > x', z = \lambda$ and $x < x', z = -\lambda$ and negative for $x < x', z = \lambda$ and $x > x', z = -\lambda$, represented by the four thin black arrows in the $z = \pm\lambda$ planes. For the non-reconnecting plane adjacent to the $z = -\lambda$ boundary, there is initially no B_y, so the presence of a $\partial B_y/\partial t$ generates a magnetic field that seeds an x-line topology (shown as an X with black dotted lines), thus promoting the spreading of the x-line in the direction of electron convection, as expected. In contrast, in the non-reconnecting plane adjacent to $z = \lambda$, $\partial B_y/\partial t$ has the opposite polarity, which serves to weaken the existing B_y, and thus the x-line and therefore reconnection do not spread in the $+z$ direction. This provides an alternate, but equivalent, understanding of why reconnection does not spread in the direction of the current in the reference frame in which the electrons carry the current.

2.3 Lack of Spreading of Anti-Parallel Reconnection in Resistive-MHD

In collisional reconnection described by resistive-MHD, the Hall, electron pressure, and electron inertia terms are dropped from the generalized Ohm's law [Eq. (2.4)]. Then, the only terms that can produce an E_x are $-v_y B_z/c, v_z B_y/c$, and ηJ_x. For anti-parallel collisional reconnection in the reference frame in which the electrons carry the out of plane current, B_z and v_z are both zero. Thus, there is no spreading in collisional reconnection due to convection in the reference frame in which the electrons carry the out of plane current. This result is consistent with previous

resistive MHD simulations (Nakamura et al., 2012), and provides a first-principles reason for the absence of spreading in this case. We point out that the resistive term, with $E_x = \eta J_x$, can in principle cause spreading. This spreading is bidirectional, as magnetic diffusion of B_y at the boundary between the reconnecting and non-reconnecting region induces an x-line topology in the non-reconnection part. Using $\Delta E_x = \Delta(\eta J_x) \sim \eta c B_y / 4\pi L_{z0}$, where L_{z0} is the length scale of the transition between the reconnecting and non-reconnecting regions, Eq. (2.2) gives

$$|v_s| \sim \frac{\eta c^2}{4\pi L_{z0}}, \tag{2.5}$$

i.e., the diffusion velocity across the boundary. This mechanism may be relevant for spreading in collisional plasmas, such as the chromosphere or some laboratory experiments. However, for most settings of heliophysical interest, the resistivity is exceedingly small, so the spreading due to resistivity is small on dynamical time scales.

2.4 Spreading of Guide Field Reconnection

The physical cause of reconnection spreading with a non-zero guide field B_{0z} is fundamentally different than with no guide field. For simplicity, we consider the limit where the guide field is much larger than the reconnecting magnetic field, $B_{0z} \gg B_0$, and that the current sheet is not sufficiently thicker than the ion gyroscale, at which point the mechanism for reconnection spreading can change because of the guide field dependence of guide field reconnection on the growth rate of the collisionless tearing

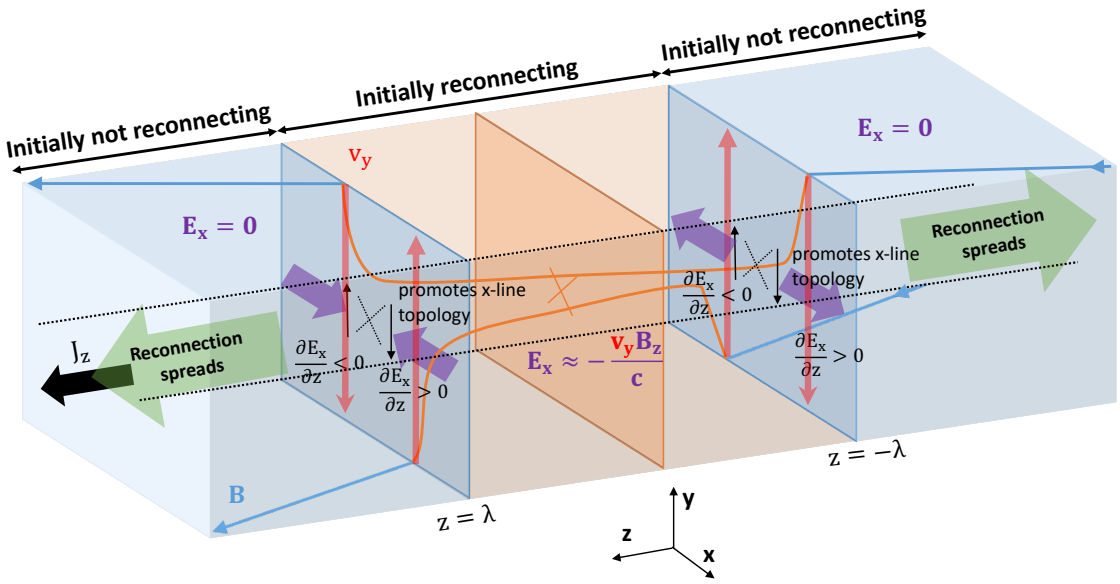

Figure 2.2 Analogously to Fig. 2.1, sketch of a system undergoing guide field reconnection in a localized region in the out of plane direction from $-\lambda < z < \lambda$, motivating the physics behind why guide field reconnection spreads bidirectionally. Reconnection between $-\lambda < z < \lambda$ convects the magnetic field towards the neutral line, which sets up a strongly bent magnetic field at the interfaces. This strong magnetic curvature drives flow in the normal direction (red arrows). This flow immersed in the guide field sets up an E_x, shown as the purple arrows. The gradient in E_x at the interfaces produces x-lines at both the $\pm\lambda$ boundaries, extending the x-line in both directions.

instability (Li et al., 2020). Figure 2.2 shows a sketch of reconnection spreading in the large guide field limit. As in Fig. 2.1, blue regions are not initially undergoing reconnection. The magnetic field in this region is shown with dark blue lines, depicted with a strong z component. The region initially undergoing reconnection with length 2λ is shown in orange. As reconnection occurs, the upstream magnetic field in this region convects inward towards the neutral line, shown in dark orange lines. This bends the upstream magnetic field, introducing a kink in the magnetic field localized near the interface of the reconnecting and non-reconnecting regions. This kinked magnetic field provides a curvature force, which drives a bulk flow in the vertical ($\pm y$) direction, depicted as red arrows near the $z = \pm\lambda$ planes. The flow, therefore, has a quadrupolar structure in the xz plane. The normal flow in a region with a guide field produces a convective electric field $E_x \approx -v_y B_z/c$, depicted by the purple arrows. It is strongest in a thin region near the interface, and also has a quadrupolar structure in the xz plane. Since E_x has a gradient in the z direction, Faraday's law implies that B_y is generated in that region, with the sign of B_y being given by Eq. (2.1). The induced B_y fields are depicted by the thin black arrows at $z = \pm\lambda$. At both edges, the magnetic topology generated by the induced B_y is of an x-line, so the x-line spreads in both out-of-plane directions. This is consistent with the known result that guide field reconnection spreads bidirectionally. We stress that this sketch of the physics is valid for both collisionless and collisional reconnection. Essentially, this bending of the magnetic field line is physically similar to a rotational discontinuity or launching an Alfvén wave. For collisionless reconnection in current sheets at gyroscales, this field line bending becomes a kinetic Alfvén wave,

as was previously elucidated (Li et al., 2020).

We now perform a scaling analysis to obtain the spreading speed in the strong guide field limit. The bulk flow in the y direction due to the curvature force from the bent upstream magnetic field is described by the momentum equation

$$\frac{\partial v_y}{\partial t} \approx \frac{B_{0z}}{4\pi m_i n}\frac{\partial B_y}{\partial z}. \tag{2.6}$$

In writing this, we use that the large guide field limit implies $v_y B_{0z} \gg v_z B_y$ in the convection electric field in Ohm's law, as both the out of plane bulk flow v_z and the reconnected field B_y are small during the early stages of reconnection.

A scaling analysis on this equation gives

$$v_y \sim \frac{B_{0z}\Delta B_y}{4\pi m_i n v_s}, \tag{2.7}$$

where we have taken $\Delta v_y \sim v_y$ between adjacent reconnecting and non-reconnecting planes and $v_s = \Delta z/\Delta t$ as per equation (2.2). Then, the relevant term in Eq. (2.4) gives E_x as

$$E_x \approx -\frac{v_y B_{0z}}{c} \sim -\frac{B_{0z}^2 \Delta B_y}{4\pi m_i n v_s c}, \tag{2.8}$$

and using this result in Eq. (2.2) reveals

$$v_s \approx \pm\left(\frac{B_{0z}^2}{4\pi m_i n}\right)^{1/2} = \pm c_{Az}. \tag{2.9}$$

This reproduces the known result that reconnection with a large guide field spreads

bidirectionally at the Alfvén speed based on the guide field c_{Az} in Eq. (1.23).

Chapter 3

Theory of Reconnection Spreading in Current Sheets of Non-Uniform Thickness

3.1 General Considerations

We now extend the theory of anti-parallel reconnection spreading developed in Chapter (2) to systems with current sheet thicknesses varying in the out of plane direction (Arencibia et al., submitted, 2022). We use the same coordinate system and reference frame established in Sec. 2.1 and assume the reconnecting magnetic field B_x asymptotes to a magnitude of B_0 at all values of z for simplicity.

We assume a model current sheet that has a half-thickness $w(z)$ in the y direction that can vary in the out-of-plane direction. A sketch of the system in the yz plane is shown in Fig. 3.1. The solid black lines represent the edge of the equilibrium current layer, and the green arrow denotes the direction that reconnection spreads due to the electron current carriers. Panel (a) denotes reconnection spreading from a thinner to thicker region of the current sheet, while panel (b) is for spreading from a thicker to thinner region. We define the current sheet half-thickness where reconnection starts as w_1 and it spreads into a region of half-thickness w_2, and we assume the transition between the two is monotonic for simplicity. We first treat spreading for which w_1 and w_2 are essentially uniform, and the region for the change

of the thickness from w_1 to w_2 is of negligible extent for simplicity, treating spreading for both thinner to thicker ($w_1 < w_2$) and thicker to thinner ($w_1 > w_2$) current sheets. Then, we treat the more physically relevant case where the half-thickness changes gradually (relative to kinetic scales).

3.2 Spreading From a Thinner to a Thicker Current Sheet

We first consider the system sketched in Fig. 3.1(a), with reconnection beginning in a region of uniform half-thickness w_1 that spreads into a thicker region of uniform half-thickness w_2, and we assume the change in half-thickness is relatively abrupt. Within the region of half-thickness w_1, previous knowledge of the spreading speed of collisionless reconnection for uniform current sheets (Huba & Rudakov, 2002; Shay et al., 2003) applies, so the spreading speed v_{s1} is

$$v_{s1} \sim \frac{J_z}{ne} \sim \frac{cB_0}{4\pi new_1} = c_A \frac{d_i}{w_1}, \tag{3.1}$$

where n is the upstream density, e is the elementary charge, $d_i = c/\omega_{pi} = (m_i c^2/4\pi ne^2)^{1/2}$ is the ion inertial scale, $c_A = B_0/(4\pi n m_i)^{1/2}$ is the Alfvén speed, and m_i is the ion mass.

The reconnected magnetic field B_{1y} in the thin region convects into the thick region by the electron current carriers (Huba & Rudakov, 2002; Shay et al., 2003). When B_{1y} reaches the thick region, it only perturbs the non-reconnecting magnetic field in the thick region over a scale with half-thickness of w_1, as marked by the dotted lines in Fig. 3.1(a), despite the full current sheet half-thickness being w_2 in

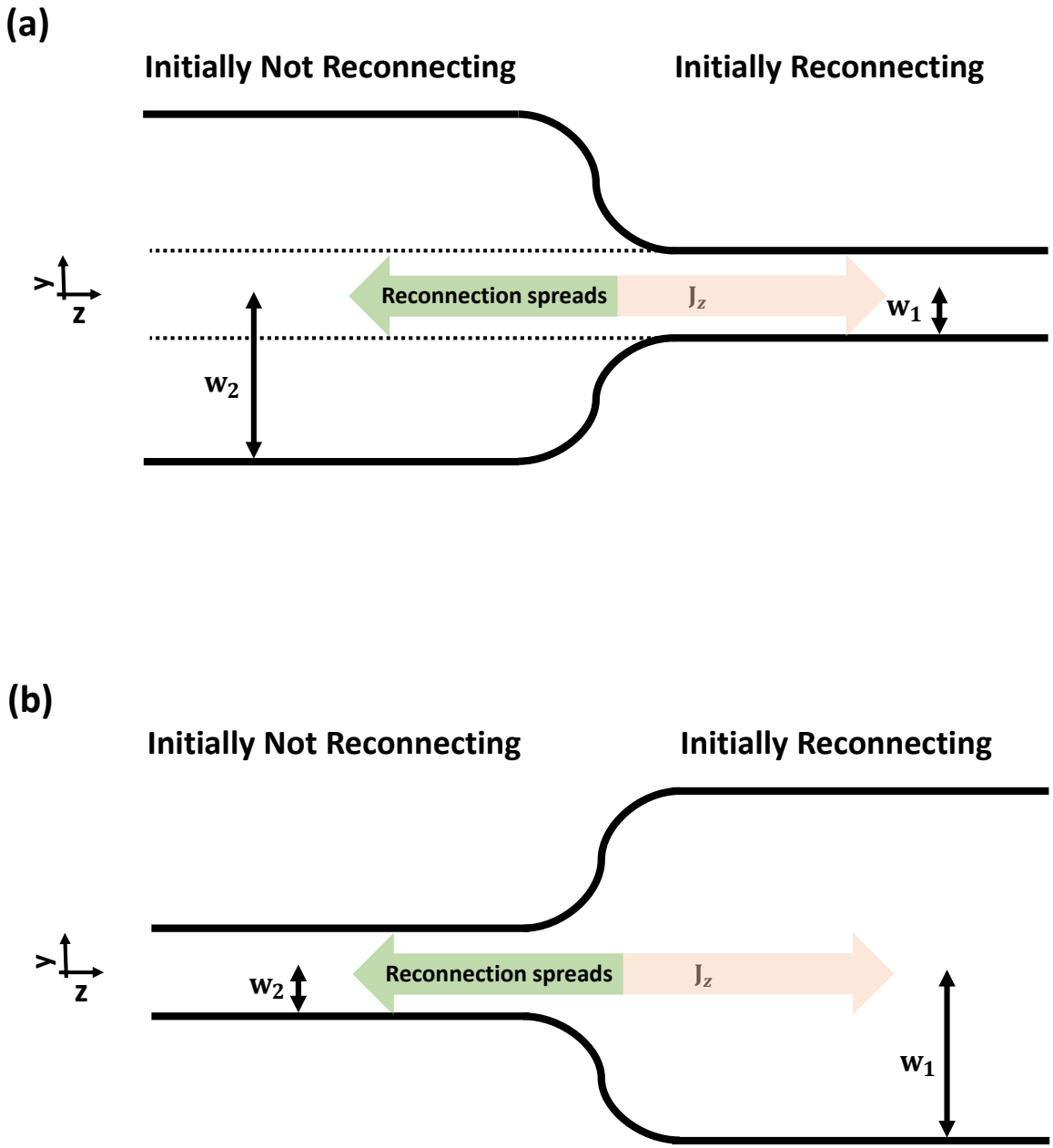

Figure 3.1 Sketch of the yz plane for a current sheet with non-uniform thickness in the out-of-plane direction in which reconnection spreads from a region of local half-thickness w_1 into a region of half-thickness w_2, propagated by the electrons carrying the current. Panel (a) is for $w_1 < w_2$ and panel (b) is for $w_1 > w_2$. The dotted lines in panel (a) denote that the reconnected fields that convect into the thicker region essentially remain collimated to a half-thickness w_1 from the thinner region, leading to embedded reconnection because the upstream magnetic field is weaker there.

this region. The magnetic field outside the region of half-thickness $y > w_1$ therefore is not significantly perturbed by B_{1y} from the thin region and does not initially participate in the reconnection in the thicker region. Consequently, the effective upstream magnetic field that controls the driving of the reconnection process is weaker than the asymptotic magnetic field B_0. Reconnection for which only a thinner sublayer participates in the reconnection process has previously been referred to as "embedded" (Shay et al., 2004; Cassak & Drake, 2009).

We estimate the spreading speed of reconnection in the thicker region by finding the reconnecting magnetic field B_{up} that initially participates in reconnection embedded in the thicker region. Assuming B_x varies approximately linearly in y within the current layer (Shay et al., 2004), we find

$$B_{up} \sim B_0 \frac{w_1}{w_2}. \tag{3.2}$$

The local spreading speed v_{s2} in the thicker region then has the same form as equation (3.1) with w_1 replaced by w_2 and B_0 replaced by B_{up}, *i.e.,*

$$v_{s2} \sim \frac{cB_{up}}{4\pi n e w_2} = c_A \frac{w_1 d_i}{w_2^2}. \tag{3.3}$$

Therefore, the predicted spreading speed v_{s2} in the thicker region is slower than the spreading speed for a current sheet of equivalent uniform half-thickness w_2, given by $c_A d_i / w_2$, by a factor of w_1/w_2. This is a key prediction of this theory and a departure from previous knowledge of reconnection spreading in current sheets of

uniform thickness. It also shows the spreading speed fundamentally depends not just on the local current sheet half-thickness w_2, but there is also a "memory" effect of the current sheet half-thickness w_1 in the thinner region.

There is a subtle point about the model presented here. Between the thin and thick parts of the current sheet, the reconnecting magnetic field has an out-of-plane gradient that is associated with an equilibrium current $J_{y,eq} = -(c/4\pi)dB_x/dz$. This implies the electrons carrying the current spread out in y as they enter the thicker region. The mechanism discussed here assumes that the reconnecting magnetic field remains collimated when it enters the thicker region, but the electron flow in y makes it seem that the reconnected magnetic field should fan out in y. The reason the equilibrium current does not typically make the reconnected magnetic field fan out in y is that the associated speeds are typically smaller than the reconnection inflow speed, so the electrons carrying the current continue to have a net flow towards the center of the current sheet. To quantify this, the vertical velocity $v_{ey,eq}$ due to the equilibrium flow scales as

$$v_{ey,eq} \sim -\frac{J_{y,eq}}{ne} \sim \frac{c}{4\pi ne}\frac{dB_x}{dz}. \tag{3.4}$$

Letting the scale over which the thickness of the current sheet changes be Δz, treating B_x to be B_0 upstream of the thin region and using equation (3.2) for the magnetic field strength $B_{up} = B_0 w_1/w_2$ at the same y location in the thick region gives

$$v_{ey,eq} \sim c_A \frac{d_i}{\Delta z}\left(1 - \frac{w_1}{w_2}\right). \tag{3.5}$$

The reconnected magnetic field remains collimated when it convects into the thick region if the reconnection inflow speed $\sim 0.1\ c_A$ exceeds $v_{ey,eq}$. This gives a condition on Δz of

$$\Delta z > 10 d_i \left(1 - \frac{w_1}{w_2}\right) \tag{3.6}$$

for the current carriers to remain collimated in the thicker current sheet. However it is unlikely that physical systems possess such steep gradients in the current sheet thickness, so we do not expect any significant influence of the equilibrium current $J_{y,eq}$ in the spreading of reconnection for typical systems.

3.3 Spreading From a Thicker to a Thinner Current Sheet

If reconnection spreads from a thick region into a thinner one as sketched in Fig. 3.1(b), the incoming reconnected magnetic field B_{1y} perturbs the entire thickness of the thinner region. The full thickness of the thinner current layer participates in reconnection from the beginning, and thus the relevant upstream magnetic field is the asymptotic magnetic field B_0. This implies that reconnection in this scenario spreads in the thinner region at a speed given by the local current carrier speed as given in equation (3.1) with w_1 replaced by w_2 but with the magnetic field strength given by B_0, *i.e.*,

$$v_{s2} \sim \frac{cB_0}{4\pi n e w_2} = c_A \frac{d_i}{w_2}. \tag{3.7}$$

Thus, in contrast to spreading from a thinner to thicker current sheet, spreading from a thicker to thinner current sheet has no memory effect and takes place at the local current carrier speed.

3.4 Spreading in a Current Sheet of Continually Varying Thickness

The results in the previous two subsections assume an abrupt change in the current sheet thickness from w_1 to w_2, but here we relax this assumption by assuming the change in thickness described by the current sheet thickness profile $w(z)$ is gradual. In this scenario, the spreading speed, which we call $v_s(z)$, is expected to be a function of z. When reconnection begins in the region of half-thickness w_1, the reconnected magnetic field convected into the thicker current sheet remains collimated at this half-thickness. This promotes reconnection in the thicker region only of magnetic fields within a half-thickness of w_1, as in the case where the half-thickness varies abruptly. Provided the time scale for spreading is shorter than the time scale for the magnetic fields outside a half-thickness of w_1 to collapse due to reconnection, the half-thickness of the reconnected field convected further down the current sheet remains collimated at a half-thickness of w_1. Consequently, the upstream reconnecting magnetic field B_{up} and the instantaneous spreading speed $v_s(z)$ are of the same form of equations (3.2) and (3.3) with w_2 replaced by $w(z)$, *i.e.,* $B_{up} \sim B_0 w_1/w(z)$ and

$$v_s(z) \sim c_A \frac{w_1 d_i}{[w(z)]^2}. \tag{3.8}$$

Similarly, for spreading from a thicker to thinner region, we expect the instantaneous spreading speed is

$$v_s(z) \sim c_A \frac{d_i}{w(z)}. \tag{3.9}$$

Since the speed is a function of position for spreading in non-uniform current sheets, it is more challenging to test the theory numerically, experimentally, or observationally by direct measurement of the speed. Thus, we also provide a prediction for the time it takes for spreading to occur over some region, which is likely to be easier to measure. From elementary mechanics, the time τ it takes to spread from position z_1 to z_2 is

$$\tau = \int_{z_1}^{z_2} \frac{dz}{v_s(z)}, \tag{3.10}$$

where the appropriate form of $v_s(z)$ from equation (3.8) or (3.9) needs to be used for thinner-to-thicker or thicker-to-thinner current sheet thickness profiles $w(z)$, respectively.

While equation (3.10) is expected to be valid for any gradually changing thickness profile $w(z)$, we exemplify the procedure by assuming a half-thickness profile $w(z)$ of the power law form

$$w(z) = w_1 + (w_2 - w_1)\left(\frac{z}{\Delta z}\right)^{\alpha}, \tag{3.11}$$

where $\Delta z = z_2 - z_1$, $z_1 = 0$, and α is a dimensionless parameter that can be chosen for a particular model current sheet. Here, $w(z_1) = w_1$ and $w(z_2) = w_2$. We first consider spreading from a thinner to thicker current sheet. Using equation (3.11) in

equation (3.8), the integral in equation (3.10) straight-forwardly gives

$$\tau = \frac{w_1 \Delta z}{c_A d_i} \left[1 + 2 \frac{w_2/w_1 - 1}{\alpha + 1} + \frac{(w_2/w_1 - 1)^2}{2\alpha + 1} \right]. \tag{3.12}$$

To interpret this result, we note from equation (3.1) that the prefactor is the transit time for reconnection spreading in a uniform current sheet of half-thickness w_1 over a distance Δz. Therefore, the α- and w_2-dependent terms in the brackets represent a geometric factor which describes the increase in the spreading time due to the current sheet becoming thicker.

Similarly, for reconnection spreading in a current sheet that decreases in half-thickness gradually from w_1 to w_2 with a profile according to equation (3.11), the local spreading speed is instead given by equation (3.9). Then, the integral in equation (3.10), after simplifying, gives

$$\tau = \frac{w_1 \Delta z}{c_A d_i} \left(1 + \frac{w_2/w_1 - 1}{\alpha + 1} \right). \tag{3.13}$$

Chapter 4

Numerical Simulation Setup

4.1 The F3D Code

We test the theory developed in Chapters 2 and 3 using 3D two-fluid and resistive-magnetohydrodynamics simulations. Simulations are carried out using the two-fluid code F3D (Shay et al., 2004), which updates the continuity, momentum, induction, and pressure equations, and can include the Hall, resistive, and electron inertia terms in the generalized Ohm's law. Time is stepped forward using the trapezoidal leapfrog algorithm (Guzdar et al., 1993) and spatial derivatives are fourth order finite differences. For simulations with the Hall term, lengths are normalized to the ion inertial scale $d_{i0} = (m_i c^2/4\pi n_0 e^2)^{1/2}$, time is normalized to the inverse ion cyclotron frequency $\Omega_{ci0}^{-1} = m_i c/eB_0$, velocities to the Alfvén speed $c_{A0} = B_0/\sqrt{4\pi m_i n_0}$, electric fields to $c_{A0}B_0/c$, and temperatures to $m_i c_{A0}^2/k_B$, where B_0 is the initial upstream reversing magnetic field magnitude, n_0 is the initial upstream density, and k_B is Boltzmann's constant. When the Hall term is absent, the only differences to the normalizations are that lengths are normalized to an arbitrary length L_{MHD}, times are normalized to L_{MHD}/c_{A0}, and resistivity is normalized to $4\pi c_{A0} L_{MHD}/c^2$.

The computational domain has dimensions $L_x \times L_y \times L_z = 102.4 \times 51.2 \times 256.0$, where x and y correspond to the outflow and inflow directions in 2D, respectively,

and z is perpendicular to the 2D reconnecting plane. Boundary conditions are triply periodic, and the system size is chosen to be large enough that the boundaries do not impact the relevant dynamics. The grid scale is $\Delta x \times \Delta y \times \Delta z = 0.05 \times 0.05 \times 1.0$. The lower resolution in the out-of-plane direction has been used before (Shay et al., 2003; Shepherd & Cassak, 2012), and is justified since out-of-plane dynamics in our setup change more slowly than dynamics in the reconnection plane. When electron inertia is included, the ion-to-electron mass ratio is $m_i/m_e = 25$, and we expect the relevant results are independent of this value, since previous work on the spreading of anti-parallel reconnection has shown that the dynamics of x-line spreading are insensitive to the mass ratio (Shay et al., 2003) and the terms in Ohm's law that contribute to reconnection spreading in the theory (the Hall and convection electric fields) are independent of the mass ratio.

4.2 Initialization and Controls

The initial conditions consist of two oppositely directed current sheets. For simulations with a uniform current sheet thickness, the x-component of the initial magnetic field is given by $B_{0x} = \tanh[(y + L_y/4)/w_0] - \tanh[(y - L_y/4)/w_0)] - 1$, where w_0 is the initial current sheet half-thickness. To validate the theory in Chapter 2, we employ simulations with uniform initial half-thickness $w_0 = 1.0$. We repeat the simulation of anti-parallel reconnection with different uniform current sheet half-thicknesses $w_0 = 0.5, 2.0$ and 3.0 and the guide field simulation with $w_0 = 2$ to confirm that in all cases, the local physics remain qualitatively similar to their

$w_0 = 1$ counterparts and that the spreading speeds are consistent with previous work (Shay et al., 2003). When a guide field B_{0z} is included, it is uniform and we use $B_{0z} = 3.0$, which is sufficient to be in the large guide field limit.

To validate the theory in Chapter 3, we employ an initial current sheet half-thickness profile $w_0(z)$ which varies in the out-of-plane direction between two specified values w_1 and w_2, given by

$$w_0(z) = \frac{w_1 + w_2}{2} + \frac{w_1 - w_2}{2}\left[\tanh\left(\frac{z + L_0}{w_z}\right) - \tanh\left(\frac{z - L_0}{w_z}\right) - 1\right], \qquad (4.1)$$

where $z = 0$ is the center of the computational domain, $L_0 = 80$ is the half-length in the out-of-plane direction of the region of half-thickness w_1, and $w_z = 4$ (unless otherwise stated) is the gradient scale length over which the half-thickness changes from w_1 to w_2. The full extent of the region over which the current sheet changes from a half-thickness of w_1 to w_2 is $\Delta z = 2w_z$, which for all simulations in this study is large enough to satisfy equation (3.6). We carry out two suites of simulations, one holding $w_1 = 1.0$ fixed and varying $w_2 = 1.25, 1.5, 1.75, 2$ (all thinner to thicker), and another holding $w_2 = 2$ fixed and varying $w_1 = 0.75, 1.5, 1.75, 1.9, 2.25, 2.5$ (a combination of thinner to thicker and thicker to thinner). We also carry out one simulation with $w_1 = 2.0$ and $w_2 = 1.5$ (thicker to thinner) and an additional two simulations with uniform half-thicknesses $w_0 = 1.0$ and 2.0. Thicker initial current sheets are desirable but, because they take longer to evolve, are significantly more computationally expensive. Fig. 4.1(a) shows initial conditions for the out-of-plane current J_z in a cut in the yz plane at $x = -L_x/2$, for a typical simulation with

non-uniform thickness showing distinct regions of different half-thicknesses $w_1 = 1$ and $w_2 = 2$ (analogous to the sketch in Fig. 3.1 in Chapter 3).

The initial density is uniform with a value of 1, and a non-uniform temperature varying from 1 to 1.5 is used to balance magnetic pressure in the current sheet. The plasma pressure is provided fully by ions and is treated as adiabatic, while the electrons are assumed cold at all times. The electrons carry all of the initial current. The resistivity η is identically zero for simulations employing the Hall term, and is 0.004 for the resistive-MHD simulations. Fourth-order diffusion is included in all equations with coefficients $D_{4x} = D_{4y} = 1.6\times10^{-5}$ and a larger diffusion coefficient in the z direction $D_{4z} = 1.6\times10^{-1}$ because the grid scale is larger. The time step is 0.02 for all simulations with no guide field. For simulations with a guide field, a smaller time step of 0.01 and a larger fourth-order diffusion coefficient $D_{4z} = 6.4 \times 10^{-1}$ are used to account for the faster dynamics in the out of plane direction. The diffusion coefficient and time step values are varied in trial simulations to ensure they do not play any significant role in the numerics.

Unless otherwise stated, we initialize the simulations with a coherent perturbation in the magnetic field. To do so, the z component of the perturbed vector potential is defined as

$$A_{1z}(x, y, z) = \frac{\tilde{B}_1 L_x}{4\pi}\left[1 + \cos\left(\frac{4\pi(y - L_y/4)}{L_y}\right)\right]\sin\left(\frac{2\pi x}{L_x}\right) f(z) \qquad (4.2)$$

for $y \geq 0$ and 0 for $y < 0$, where $\tilde{B}_1 = 0.005$ is a constant and the envelope $f(z)$ has

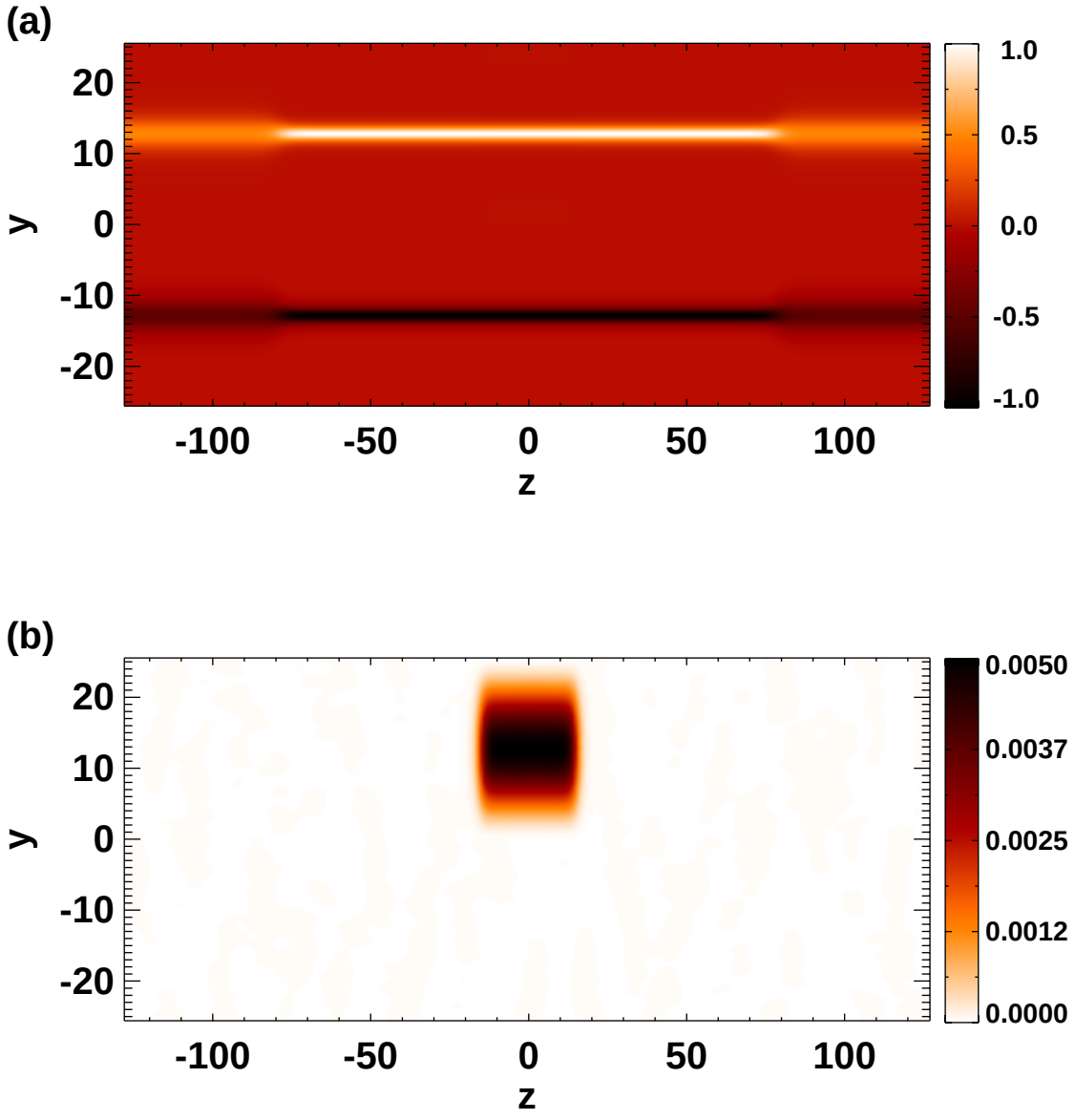

Figure 4.1 Representative initial conditions for a simulation with a current sheet with thickness that varies in the out-of-plane direction. The plots give a cut in the yz plane at $x = -L_x/2$ of (a) the initial current density J_z with a thickness profile given by equation (4.1) with $w_1 = 1$ and $w_2 = 2$, and (b) the y-component of the magnetic perturbation B_{1y}.

the form

$$f(z) = \frac{1}{2}\left[\tanh\left(\frac{z + w_{0pert}}{2}\right) - \tanh\left(\frac{z - w_{0pert}}{2}\right)\right], \tag{4.3}$$

where w_{0pert} defines the initial half-extent of the coherent perturbation in the out of plane direction. We use $w_{0pert} = 15$ unless stated otherwise. The resulting magnetic perturbation $\mathbf{B}_1 = -\hat{\mathbf{z}} \times \nabla A_{1z}$ seeds an x-line/o-line pair in the xy plane for only the upper current sheet at $y = y_{cs} = L_y/4$, localized to $-w_{0pert} < z < w_{0pert}$. Figure 4.1(b) shows a cut in the yz plane at $x = -L_x/2$ of the y-component of the coherent perturbation in the magnetic field. For simulations with non-uniform current sheet thickness, the value of w_{0pert} is chosen to ensure the perturbation is localized exclusively in the region of half-thickness w_1 so that any reconnection observed in the region of half-thickness w_2 is due to spreading of reconnection and not due to the initial perturbation. We perturb only the upper current sheet because doing so prolongs the timescale for the interaction between the two current sheets due to flows in the y-direction and thus ensures the reconnection occurring in the upper sheet at later times is purely due to reconnection spreading in the upper sheet. In all simulations, incoherent noise in the x and y components of the magnetic field at the 10^{-5} level is also used to break symmetry, which prevents secondary magnetic islands from staying in the initial x-line location (Shay et al., 2004).

To ensure the spreading has no dependence on w_{0pert}, we perform a suite of simulations with an anti-parallel field configuration with $w_0 = 1$ with varying w_{0pert} of $9, 12, 15$, and 30, with all other parameters held the same. We find that w_{0pert} affects the initial extent of the reconnection region in the z direction at the time of

onset, which is to be expected, but the spreading of reconnection is unaffected.

Chapter 5

Numerical Results and Theory Validation

5.1 Validation of Anti-Parallel Collisionless Reconnection Spreading Model

We begin by testing the model of collisionless anti-parallel reconnection spreading in Chapter 2. To do so, we need to verify the structure and the dominant contributor of the electric field E_x and the time evolution of the magnetic field B_y near the boundary of the initial reconnecting region.

We investigate the electric and magnetic field structure at $t = 10$, when the perturbed B_y is spreading out from its initial location, but before full-fledged reconnection is going at its steady rate (which occurs closer to $t = 80$), as discussed in Section 2.1. Figure 5.1 shows the net electric field component E_x. Planar cuts through the upper (perturbed) current sheet $y = y_{cs} = 12.8$ and through the reconnecting planes at $z = 2$ and $z = -20$ near the boundaries of where reconnection occurs are shown. These z planes are selected because the x-line seeded by the perturbation is initially between $z = \pm 15$, but this region drifts in the $-z$ direction, the direction of electron convection. The initial convection of the perturbed region before reconnection spreads is consistent with the behavior observed in Fig. 1 of Huba & Rudakov (2002), though it was not discussed in their study.

Anti-Parallel	$(x=-38.4, 2<z<10)$	$(x=-38.4, -28<z<-20)$	$(x=-12, 2<z<10)$	$(x=-12, -28<z<-20)$
$-\frac{\partial E_x^{Hall}}{\partial z}$	-0.00045	0.00045	0.00048	-0.00048
$\frac{\partial B_y}{\partial t}$	-0.00056	0.00058	0.00056	-0.00056

Table 5.1 Comparison of the out of plane gradient of the Hall electric field $-\partial E_x^{Hall}/\partial z$ and the local time derivative $\partial B_y/\partial t$ for the $w_0 = 1$ anti-parallel collisionless reconnection simulation at $t = 10$. The spatial gradient is measured over the specified ranges in z near the boundaries of the reconnecting region, and the time derivative is measured between $t = 9$ and 11 at the midpoint of the specified ranges in z. The agreement confirms that the electrons convect the x-line topology in the $-z$ direction for anti-parallel reconnection.

Guide Field 3	$(x=-38.4, 38<z<48)$	$(x=-38.4, -48<z<-38)$	$(x=-12, 38<z<48)$	$(x=-12, -48<z<-38)$
$-\frac{\partial E_x^{conv}}{\partial z}$	0.00050	0.00026	-0.00053	-0.00027
$\frac{\partial B_y}{\partial t}$	0.00041	0.00035	-0.00043	-0.00038

Table 5.2 Same as Table 5.1, but for the convective electric field at the given locations and times in the guide field 3 case. The agreement confirms that the convection electric field gradients propagate the x-line topology in the $\pm z$ directions for guide field reconnection.

The red-white-blue color map for the electric field E_x ranges from -0.005 to 0.005. The two zeroes of E_x in the reconnecting region (in white) at $x = x' = -25.6$ and $x = 25.6$ coincide with the x-line and o-line, respectively. The electric field E_x is qualitatively similar at later times when the x-line is significantly longer in extent in the $-z$ direction. The bipolar structure of E_x points outwards from the x-line, consistent with the sketch in Fig. 2.1. The largest contributor to E_x is the Hall term $E_x^{Hall} = -J_z B_y/nec$, as expected (Huba & Rudakov, 2002). It has a maximum magnitude of 0.005 and is two orders of magnitude larger than the next largest contribution from the convection term $v_z B_y/c$.

To quantitatively confirm that the induction of B_y is caused by E_x^{Hall}, we compute the out of plane gradient $\partial E_x^{Hall}/\partial z$ at both boundaries of the reconnecting region to the left and right of the initial x-line, $x = -38.4$ and $x = -12$, respectively. We use least squares to fit a line to E_x^{Hall} as a function of z through the center line

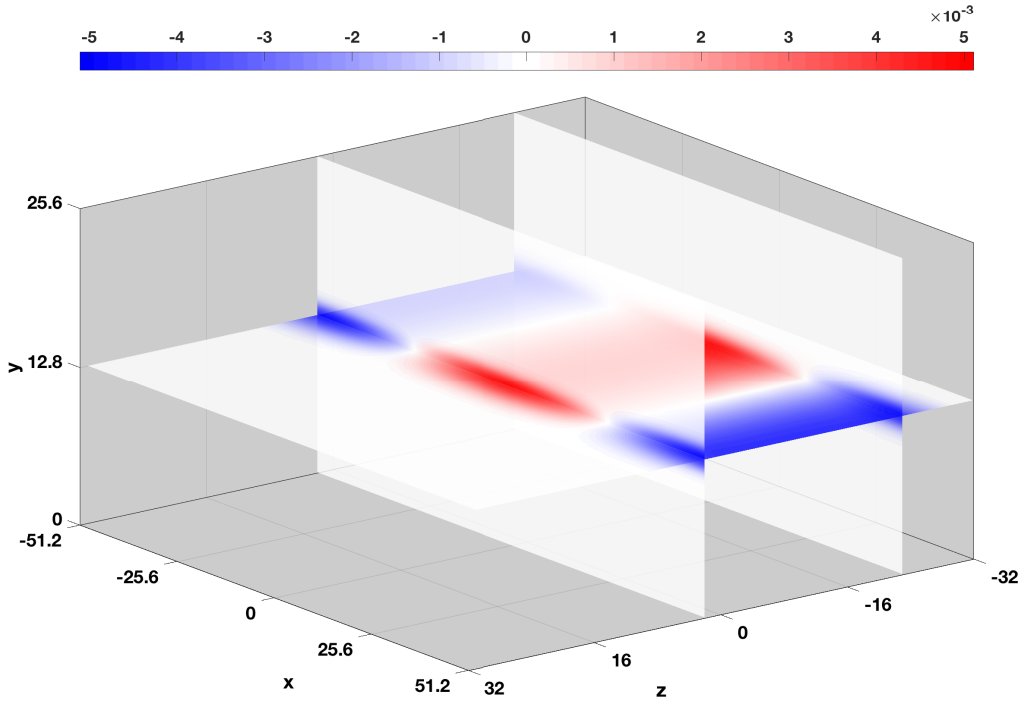

Figure 5.1 Electric field E_x from a 3D simulation of anti-parallel reconnection with a current sheet of initial thickness 1 at $t = 10$. Data are plotted at planes of $y = y_{cs} = 12.8$, $z = 2$, and $z = -20$. The x-line is at $x = -25.6$, and the o-line is at $x = 25.6$. The structure of E_x is consistent with the sketch in Fig. 2.1, motivating why anti-parallel reconnection spreads only in the direction of the current carriers.

of the upper current sheet from $-28 < z < -20$ and $2 < z < 10$ to approximate $\partial E_x^{Hall}/\partial z$. We calculate the local time derivative $\partial B_y/\partial t$ at the midpoint of the specified ranges in z, determined with a time-centered difference between $t = 9$ and 11. The results are gathered in Table 5.1. The similarity between the two terms shows that the main contribution to $\partial B_y/\partial t$ comes from $-\partial E_x^{Hall}/\partial z$, as expected.

The signs of $\partial B_y/\partial t$ in the $z = -24$ plane are negative at $x = -12$ and positive at $x = -38.4$, to the left and right of the zero of B_y, respectively. This serves to promote an x-line topology in the $z = -24$ plane. In contrast, at $z = 6$, the signs of $\partial B_y/\partial t$ oppose the formation of an x-line, consistent with our explanation of why reconnection does not spread in the z direction. These results confirm our theoretical predictions for anti-parallel collisionless reconnection spreading discussed in Section 2.2.

5.2 Validation of Guide Field Collisionless Reconnection Spreading Model

We now validate the model of collisionless guide field spreading in the large guide field limit discussed in Chaper 2. Figure 5.2 shows the net electric field component E_x at $t = 10$ for a simulation with guide field $B_{0z} = 3$, again when the perturbed B_y is spreading out from its initial location, but before full-fledged reconnection is going at its steady rate. Planar cuts are shown at $y = y_{cs}$ through the upper (perturbed) current sheet and the $z = -38$ and $z = 38$ planes near the boundaries between the reconnecting and non-reconnecting regions. The two zeroes

of E_x at the intersections of the planes (in white) are again located at approximately $x = x' = -25.6$ and $x = 25.6$, coinciding with the x-line and o-line, respectively. Note, E_x has a much larger extent in the y direction than for the anti-parallel case, which is localized within an ion inertial scale. That E_x extends far beyond the current sheet to MHD scales is typical of reconnection with a large guide field. When reconnection is occurring, ion inflows v_y extend into the upstream region, well outside the current layer to MHD scales. In the absence of a guide field B_{0z}, the associated convection electric field $E_x \sim v_y B_z/c$ in the upstream region is negligible. This is because the only contribution to B_z is the quadrupolar Hall magnetic field, which is very small at MHD scales upstream of the diffusion region. This explains why E_x is localized to the current layer in the case without a guide field (see Fig. 5.1). However, if there is a large guide field B_{0z}, the electric field $E_x \sim v_y B_z/c$ is non-zero, both at Hall scales and beyond the current layer into MHD scales because of the ion inflow, as is seen in Fig. 5.2

The largest contributor to the electric field E_x during the initial spreading phase is the convection term $E_x^{conv} = v_y B_z/c$, which has a maximum magnitude of 0.009 and is three times larger than than the next largest contribution from $E_x^{Hall} = J_z B_y/nec$. The quadrupolar structure of E_x points inwards towards the x-line at $z = 38$ and outwards from the x-line at $z = -38$, consistent with the sketch in Fig. 2.2.

We note that there is a small amplitude oscillatory signature at the leading edges of the E_x signal. This is reminiscent of low amplitude oscillatory behavior observed in the study by Jain & Büchner (2017) in the outermost edges of the

reconnecting region, although in our simulation we do not see the larger amplitude oscillations they observed in between. Understanding these differences is outside of the scope of the present study. Regardless, due to the smallness of this oscillatory signal in our study (~ 0.001 compared to ~ 0.008 for the non-oscillatory signal), it is not playing any significant role in the spreading. To quantitatively confirm the induction of B_y is caused by the convective electric field, we compute $\partial E_x^{conv}/\partial z$ at both boundaries of the reconnecting region to the left and right of the initial x-line, $x = -38.4$ and $x = -12$ respectively, using a similar approach as the previous section, at $-48 < z < -38$ and $38 < z < 48$. We then compare to $\partial B_y/\partial t$ at the midpoint of the specified ranges $z = -43$ and $z = 43$, computed as in the previous section. The results are gathered in Table 5.2. The similarity between the two quantities shows that the main contribution to $\partial B_y/\partial t$ comes from $-\partial E_x^{conv}/\partial z$, as we predict in our scaling of Eq. (2.8) for the large guide field limit. The signs of $\partial B_y/\partial t$ show that B_y develops with a negative sign at $x = -38.4$ and a positive sign at $x = -12$, to the left and right of the zero of B_y, respectively, at both $z = -42$ and $z = 42$. This implies the magnetic topology is that of an x-line at both $z = -42$ and $z = 42$ planes, consistent with the model for why the x-line spreads in both the z and $-z$ directions.

Additionally, we test the prediction that the bulk flow v_y is driven by the curvature force due to the bent upstream magnetic field at the boundaries of the reconnecting region by directly computing the left and right hand sides of Eq. (2.6) with simulation data. For the right hand side, we first compute $\partial B_y/\partial z$ at $t = 10$ near the ends of the reconnecting region through $y = y_{cs}$, using a least squares fit of

Momentum Eqn.	$(x=-38.4, 35<z<42)$	$(x=-38.4, -42<z<-35)$	$(x=-12, 35<z<42)$	$(x=-12, -42<z<-35)$
$\left(\frac{B_z}{n}\right)\frac{\partial B_y}{\partial z}$	-0.00021	0.00024	0.00026	-0.00043
$\frac{\partial v_y}{\partial t}$	-0.00021	0.00014	0.00023	-0.00045

Table 5.3 Comparison of the curvature force term $(B_z/n)\partial B_y/\partial z$ (in code units) and the local acceleration of the bulk flow $\partial v_y/\partial t$, in the guide field reconnection spreading simulation at $t = 10$. The spatial derivative is averaged over the given ranges in z near the boundaries of the reconnecting region, and the time derivative is determined from a time-centered difference between $t = 9$ and 11 at the midpoint in the specified ranges in z. This confirms that the curvature force drives the vertical flows.

B_y as a function of z from both $-42 < z < -35$ and $35 < z < 42$ and to the left and right of the x-line at $x = -38.4$ and $x = -12.8$, respectively. Then, the numerical estimate for the curvature force term is $(B_z/n)\partial B_y/\partial z$ (in code units). The left hand side $\partial v_y/\partial t$ is then computed locally at the midpoints $z = 38$ and $z = -38$ with a time-centered difference between $t = 9$ and 11. The results are gathered in Table 5.3. The similarity of the two terms is strong evidence that the curvature force drives the bulk flows v_y near the boundaries of the reconnection region in guide field reconnection. In summary, our simulation results confirm the predictions about the electric and magnetic fields in guide field reconnection in Section 2.4.

5.3 Spreading of collisional reconnection in resistive-MHD

Here, we study the spreading of collisional reconnection in resistive-MHD to test the predictions in Section 2.3. For these simulations, the initial out-of-plane length scale in z of the transition is $L_{z0} = 2$ from Eq. (4.3) and $\eta = 0.004$, so Eq. (2.5) gives a predicted spreading speed of $v_s \simeq 0.002$ (in code units). For the duration of the simulations carried out here, the distance reconnection would spread from resistive effects is expected to be negligible. Consequently, we expect no spreading

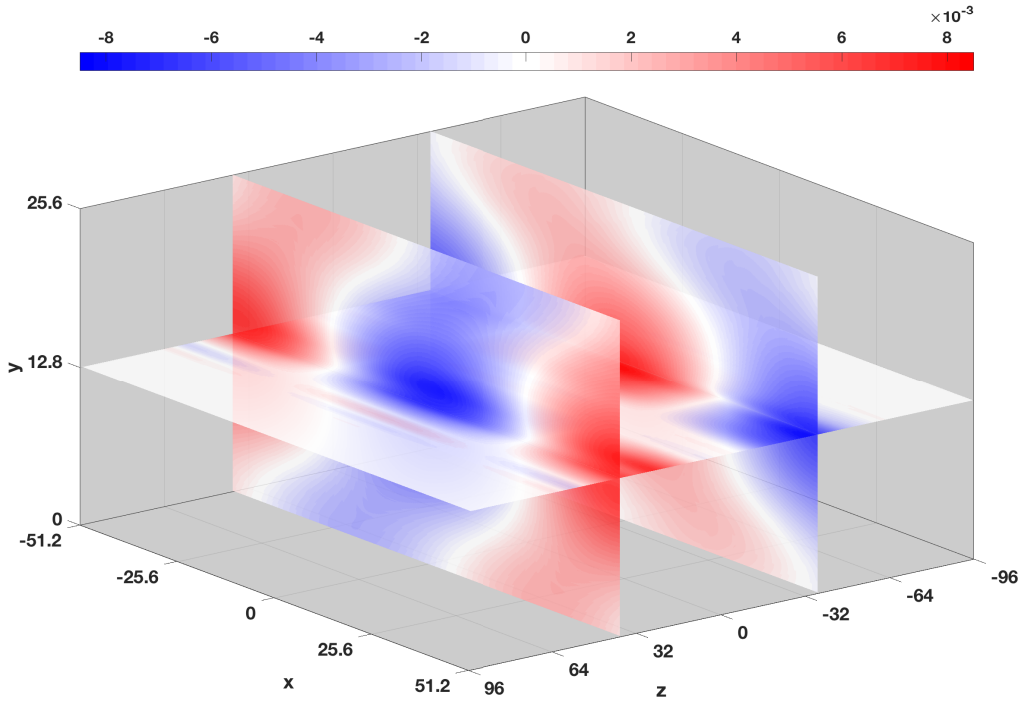

Figure 5.2 Electric field E_x from a 3D simulation of guide field reconnection with a guide field 3 with a current sheet of initial thickness $w_0 = 1$ at $t = 10$. Data are plotted at planes of $y = y_{cs} = 12.8$, $z = -38$, and $z = 38$. The x-line is at $x = -25.6$, and the o-line is at $x = 25.6$. The structure of E_x is consistent with the sketch in Fig. 2.2, motivating why reconnection spreads bidirectionally.

for anti-parallel reconnection, but spreading will occur for guide field reconnection.

We carry out two 3D simulations using the resistive-MHD model. One has no guide field, and one has guide field $B_{0z} = 3$. The initial current sheet thickness is $w_0 = 0.32$. All other system properties and initialization parameters are the same as described in Chapter 4. For the anti-parallel reconnection simulation, we find that reconnection does not spread up to the simulated time $t = 200\ L_{MHD}/c_{A0}$ (not shown). If spreading were to occur at the speed of the current carriers $v_s = J_z/ne = 1/w_0 \approx 3\ c_{A0}$, we would expect reconnection would spread a distance $\approx 600\ L_{MHD}$ in the simulated time. This would be clearly observable, as this is longer than the computational domain in the z direction. The region undergoing reconnection also does not convect in the out of plane direction, as the electrons initially carry all the current. These findings are consistent with previous results (Nakamura et al., 2012). With $B_{0z} = 3$, reconnection spreads bidirectionally (not shown), as in the collisionless two-fluid simulation. This confirms that, for the parameters of our study, there is no spreading for anti-parallel reconnection in which electrons carry the current within the resistive-MHD model, that MHD physics drives the spreading when there is a guide field, and that collisions play no important role in reconnection spreading.

5.4 Dependence of spreading on system aspect ratio

An interesting result arises from comparing our anti-parallel collisionless reconnection simulation with $w_0 = 2$ (used to confirm the results from the $w_0 = 1$

simulation do not depend on the current sheet thickness) with previous knowledge. In particular, we find that reconnection spreads with $w_0 = 2$, while a previous study found that reconnection with a current sheet of that thickness developed a reconnecting region of finite extent in the z direction and simply convected at the speed of the current carriers rather than spread (Shay et al., 2003); see the dashed lines of their Fig. 3a. Similar behavior was observed in other studies of Hall reconnection spreading in relatively thick current sheets (Meyer III, 2013).

The difference between the present and previous simulations is that the prior studies used a square computational domain in the $xy-$plane, whereas our domain is twice as big in the x direction than in the y direction. We repeat our simulation with a current sheet of thickness $w_0 = 2$ in a square computational domain with $L_x \times L_y \times L_z = 51.2 \times 51.2 \times 256.0$, as in Shay et al. (2003). We also find the x-line remains a fixed length and convects rather than spreads.

We demonstrate our result graphically using a plot of the reconnected magnetic field B_y. For a given xy plane we find the reconnection region by first finding the zeroes of B_y through the symmetry line of the current sheet in the $y = y_{cs} = L_y/4$ plane and determine if the magnetic topology is that of an x-line or an o-line. For a current in the z direction, B_y changing from positive to negative with increasing x is an x-line and from negative to positive is an o-line. If there are multiple x-lines, we define the primary one as that with the largest out-of-plane current J_z. The strength of the reconnected field B_y increases from zero away from the reconnection region until the downstream edge of the electron diffusion region. At every plane of constant z and at every time t, we use the average magnitude of B_y at the left and

right downstream edges of the electron diffusion region as a proxy for the appearance of reconnection and denote this quantity as $\tilde{B}_y(z,t)$.

For the distance from the x-line to the downstream edges of the electron diffusion region, we note that the collisionless reconnection rate E is typically ~ 0.1 [*e.g.*, (Shay et al., 1999b; Birn et al., 2001; Liu et al., 2017)], which is also comparable to the aspect ratio of the diffusion region δ/L, where δ is its thickness (in the y direction) and L is its length (in the x direction). The thickness of the electron diffusion region (Vasyliunas, 1975) is the electron inertial scale d_e, so one expects the length L of the electron diffusion region to be approximately 10 d_e. For this study, $L \approx 2\ d_{i0}$ since $d_e = 0.2\ d_i$. We validate this choice by visual inspection of cuts of B_y, confirming this choice of L reasonably represents where the strength of the reconnected magnetic field is near its first maximum. Consequently, we compute the average reconnected field magnitude $\tilde{B}_y(z,t)$ at the downstream edges of the electron diffusion region for each xy plane as

$$\tilde{B}_y(z,t) = \frac{|B_y\left(x' + L, y_{cs}, z, t\right)| + |B_y\left(x' - L, y_{cs}, z, t\right)|}{2}, \tag{5.1}$$

where x' is the location of the x-line in the plane in question.

The average reconnected field $\tilde{B}_y(z,t)$ for the upper current sheet $y = y_{cs} = L_y/4$ is shown as a stack plot of time t and out-of-plane coordinate z for the rectangular computational domain in Fig. 5.3. The time delay between the spreading of B_y and the onset of full-fledged reconnection is apparent as the white space on the left side of the plot; the reconnection does not begin at $z = -45$ until $t \approx 170$

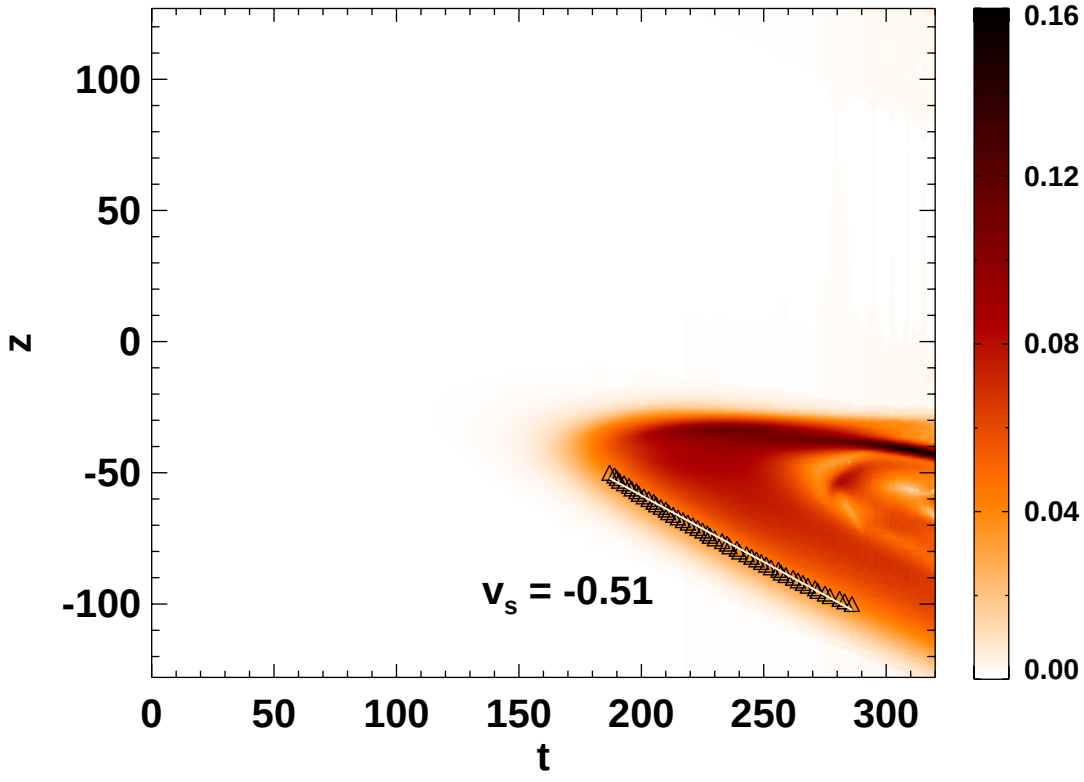

Figure 5.3 Average reconnected magnetic field $\tilde{B}_y(z,t)$, defined in Eq. (5.1), as a function of out of plane position z and time t, for the anti-parallel reconnection simulation with $w_0 = 2$. The triangles mark where $\tilde{B}_y$ crosses over 0.04, and the white line gives the best fit of these points, giving the spreading speed v_s. This plot shows reconnection spreads, in contrast to the results in a square computational domain in which the x-line convects without spreading [Fig. 3a of Shay et al. (2003)].

even though the perturbed B_y would have reached that location by $t = 60$. The triangular shape of $\tilde{B}_y(z,t)$ is representative of reconnection that is spreading, and not convecting with a fixed extent. A reconnecting x-line that is merely convecting without spreading would appear as a diagonal stripe, with a fixed extent in the z-direction. An example of this is in Fig. 3(a) of Shay et al. (2003); the dashed lines there show a reconnecting x-line that convects with a fixed length. The interior structures within the overall triangular region are due to magnetic islands that arise after reconnection at that location has reached its steady state. To calculate the spreading speed, we define onset at a given xy plane to be when $\tilde{B}_y$ exceeds 0.04. Onset times for individual xy planes are plotted in Fig. 5.3 as black triangles for a chosen interval in $-100 < z < -50$. The spreading speeds are simply the slope of the collection of points denoting the onset time. We determine this slope using a least squares fit. We find the spreading speed is $v_s \approx -0.51$, consistent with Eq. (1.22), as expected. Moreover, in a separate simulation with $w_0 = 3$ with the same square domain, we find that fast reconnection does not occur in the simulated time, whereas reconnection does occur in the rectangular cross section domain and spreads at the current carrier speed rather than merely convecting.

These results suggest that the aspect ratio of the reconnecting plane of the computational domain contributes to whether reconnection spreads or convects. We hypothesize that reconnection in the square domain stops because the reconnection runs out of free magnetic energy relatively quickly, while in the rectangular domain there is more free energy and thus the reconnection persists longer, consistent with the stack plot. This is only a single simulation, though, so future work is needed to

test this hypothesis.

5.5 Dependence on perturbation structure

To test whether the results obtained here are dependent on the manner in which reconnection is initiated in the system, we carry out an anti-parallel reconnection simulation with current sheet thickness $w_0 = 1$, with the Hall effect and electron inertia turned on. Instead of perturbing the current sheet with a coherent perturbation of the magnetic field [see Eq. (4.2)], we perturb the system with localized regions of higher plasma pressure localized just upstream of the current sheet. This perturbation is designed to drive flow towards the current sheet in a localized region to seed an x-line. The pressure perturbation P_1 we employ has the form

$$P_1(x,y,z) = P_{i1} \exp\left\{-0.5\left[\left(\frac{x-x'}{w_{0x}}\right)^2 + \left(\frac{y-y_{cs}-y_{0pert}}{w_{0y}}\right)^2 + \left(\frac{y-y_{cs}+y_{0pert}}{w_{0y}}\right)^2\right]\right\} f(z), \tag{5.2}$$

where $P_{i1} = 2$ is the amplitude of the upstream pressure perturbation, $x' = -L_x/4$ is the desired x coordinate of the x-line, $w_{0x} = 4$ is the extent of the pressure perturbation in the x direction, $y_{cs} = L_y/4$ is the y location of the center of the current sheet being perturbed, $w_{0y} = 1$ is the thickness of the pressure perturbation in the y direction, $y_{0pert} = 4$ is the distance upstream of the current layer on each side that the pressure perturbation is centered, and $f(z)$ is the same envelope in Eq. (4.3) enforcing localization in z between $\pm w_{0pert}$.

The pressure perturbation launches a pulse that propagates out in all directions. The ion pressure P_i in a cut through $y = y_{cs}$ at $t = 20$ is shown in Fig. 5.4(a). The leading edge of the pressure pulse at this time is at $z \approx \pm 50$, so its velocity is approximately 35 / 20 $\approx$ 1.75. This compares favorably to the fast magnetosonic speed, $v_{ms} = (c_A^2 + c_s^2)^{1/2} = (1 + 5/3)^{1/2} = 1.63$, as expected. The pressure pulse drives flow toward the current sheet which initiates reconnection, as desired, and the reconnection does spread in time. The reconnected magnetic field B_y in the same plane at the same time is shown in Fig. 5.4(b). The figure shows that reconnection spreads unidirectionally in the direction of the current carriers, not bidirectionally. The average reconnected field $\tilde{B}_y(z,t)$ at $y = y_{cs}$ is shown as a stack plot in Fig. 5.5. Using the same method described in Sec. 5.4, the reconnection spreading velocity is found to be ≈ -0.92, represented as a white line. This is consistent with the velocity of the current carriers, which is -1 for this simulation. For reference, two dashed black lines are sketched representing what the boundaries of the structure in the stack plot would be if reconnection were to spread bidirectionally at the fast magnetosonic speed $v_{ms} \approx \pm 1.63$, showing clear disagreement.

We conclude that perturbing the current sheet using a coherent perturbation in the magnetic field does not introduce a bias in our theoretical model for anti-parallel reconnection spreading, at least for the simulation presented here. More research is needed to see whether there are scenarios in which reconnection can spread with the fast magnetosonic speed, as has been previously suggested (Vorpahl, 1976).

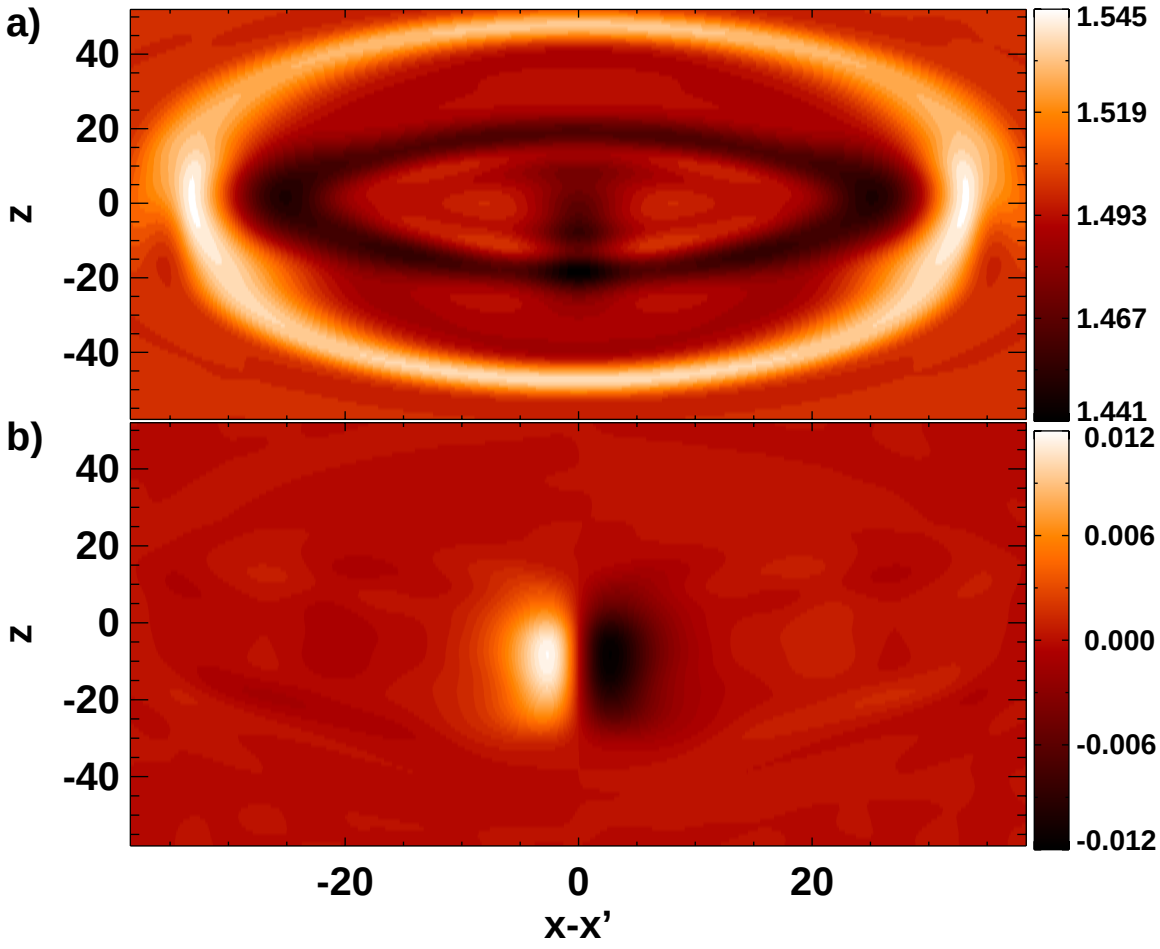

Figure 5.4 Planar cuts through $y = y_{cs}$ from a 3D simulation of anti-parallel Hall reconnection with a current sheet of initial thickness $w_0 = 1$ at $t = 20$. This simulation seeds reconnection with a pressure pulse instead of a magnetic perturbation. (a) Ion pressure P_i and (b) reconnected magnetic field B_y. The pressure pulse propagates bidirectionally at the fast magnetosonic speed, but reconnection spreads in the direction of the current carriers in the current sheet.

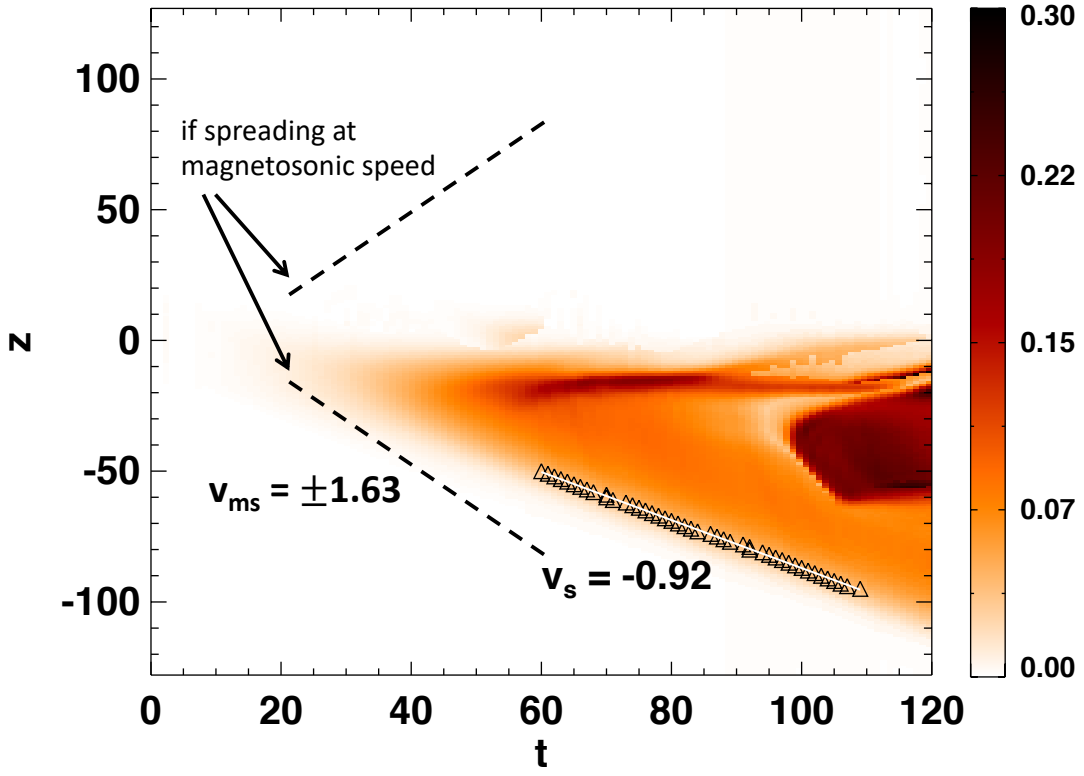

Figure 5.5 Average reconnected magnetic field $\tilde{B}_y(z,t)$, defined in Eq. (5.1), as a function of out of plane position z and time t, for the anti-parallel reconnection simulation with $w_0 = 1$ initiated with a pressure perturbation. Dashed lines show the expected x-line bounds if spreading occurs bidirectionally at the fast magnetosonic speed v_{ms}. Instead, spreading occurs unidirectionally with electron flow speed v_s in the current sheet, denoted by the white line.

5.6 Validation of Spreading Model in Non-Uniform Current Sheets

We now test the model of anti-parallel collisionless reconnection spreading in non-uniform current sheets discussed in Chapter 3 by testing the spreading speed prediction in equations (3.3) and (3.7). We generate time-distance stack plots of the averaged reconnected magnetic field $\tilde{B}_y(z,t)$ and use them to calculate the reconnection spreading speed for each of the simulations with non-uniform current sheet thicknesses, using the same method discussed in Sec. 5.4.

The average reconnected field $\tilde{B}_y(z,t)$ for the upper current sheet ($y = y_{cs} = L_y/4$) is shown in Fig. 5.6 as a stack plot as a function of time t and out-of-plane coordinate z over the whole domain for four 3D simulations with non-uniform thickness. Panels (a) through (d) have $w_2 = 1.25, 1.5, 1.75$, and 2.0 in the thicker part of the current sheet, respectively, and all four have $w_1 = 1$ in the thinner part. Each horizontal cut represents data from a fixed xy plane as a function of time t, while each vertical cut represents the spatial extent of $\tilde{B}_y$ in the z direction of the reconnecting region at a fixed time. We see $\tilde{B}_y$ increase in time from 0 to an asymptotic value of ≈ 0.1 when reconnection reaches a quasi-steady state in the current sheet region with local half-thickness w_1 before spreading in the $-z$ direction into the region with local half-thickness w_2.

As in Sec. 5.4, we define the onset of fast reconnection at a given xy plane to be when $\tilde{B}_y$ exceeds 0.04, after which reconnection proceeds to a quasi-steady state. Onset times for individual xy planes are plotted in Fig. 5.6 as black triangles for a chosen interval in z in the region of initial half-thickness w_2. We determine this

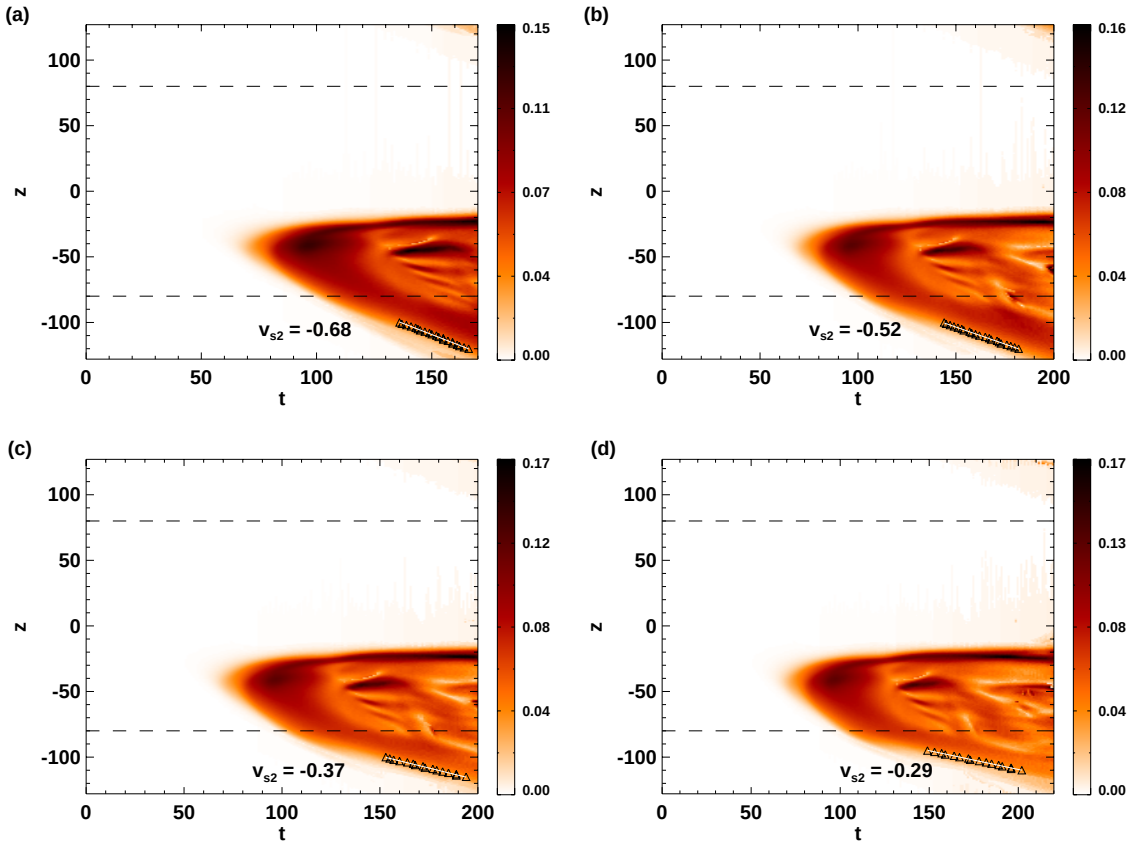

Figure 5.6 Average reconnected magnetic field $\tilde{B}_y(z,t)$, defined in equation (5.1), plotted as a function of the out-of-plane direction z and time t, for simulations with initial non-uniform current sheet half-thicknesses $w_1 = 1$ for $-80 < z < 80$ and opening out to $w_2 =$ (a) 1.25, (b) 1.5 (c) 1.75, and (d) 2 elsewhere separated by dashed lines, where distances are in units of d_{i0} and times are in Ω_{ci0}^{-1}. Black triangles denote when and where $\tilde{B}_y = 0.04$ for a chosen range in z in the region of initial half-thickness w_2. The out-of-plane reconnection spreading speed v_{s2} in the region with half-thickness w_2, listed for each simulation in units of c_{A0}, is the best fit slope of these points, shown as a white line.

slope using a least squares fit and the slopes are shown as the white lines in each panel of Fig. 5.6. The spreading speed in the region of half-thickness $w_1 = 1$ for all four simulations in Fig. 5.6 are $v_{s1} \simeq 1.0$ (not shown), which is consistent with equation (3.1) as expected (Huba & Rudakov, 2002; Shay et al., 2003). In all four cases, there is a break in the spreading speed where the reconnection reaches the region of larger half-thickness w_2 and all show spreading speeds well below the local current carrier speed $c_{A0}d_{i0}/w_2$.

Stack plots analogous to those in Fig. 5.6 are generated and spreading speeds are obtained using the same method for all the simulations in this study (not shown). Table 5.6 gathers the results for all simulations in this study in the first column, labeled as ordered pairs (w_1, w_2) according to their respective current sheet half-thicknesses. We include the spreading speed prediction from equations (3.3) and (3.7) in the region of half-thickness w_2 in the second column for simulations with $w_1 < w_2$ and $w_1 > w_2$, respectively. The third column is the calculated spreading speed magnitude v_{s2} from the simulations and the fourth column is the deviation from the theoretical prediction shown as a percentage.

We gather the spreading speeds from our simulations in Fig. 5.7. Panel (a) shows v_{s2} as a function of the current sheet half-thickness w, which represents either independent variable w_1 or w_2, depending on which is the independent variable for the given set of simulations. The two uniform half-thickness simulations $(w_1, w_2) = (1, 1)$ and $(2, 2)$ are shown as blue crosses. The three simulations with $w_1 = 1$ and $w_2 = 1.25, 1.5, 1.75$ are shown as black squares and the independent variable is $w = w_2$. The five simulations with $w_1 = 0.75, 1.0, 1.25.1.5, 1.75, 1.9$ and $w_2 = 2$

are shown as red triangles and the two simulations with $w_1 = 2.25, 2.5$ and $w_2 = 2$ are shown as red asterisks, where the independent variable is $w = w_1$. The dashed black line represents the theoretical prediction from equation (3.3) for simulations with $w_1 = 1$ fixed with $w = w_2$ as the independent variable. The red dash-dot piecewise-curve represents the prediction from equation (3.3) with $w_2 = 2$ fixed with $w = w_1$ as the independent variable for $w_1 < w_2$, and equation (3.7) for $w_1 > w_2$. The simulation results are in excellent agreement with the theory. The $(w_1, w_2) = (2, 1.5)$ simulation is not expected to lie on either of the two curves and thus is not shown.

To test the agreement more quantitatively, Fig. 5.7(b) shows spreading speeds v_{s2} for all simulations with $w_1 \leq w_2$ as a function of w_1/w_2^2, the predicted dependence from equation (3.3). We calculate a linear least squares fit of these points and show the fit as a dashed line with a functional form $(0.919 \pm 0.082) w_1/w_2^2 + (0.044 \pm 0.041)$, showing excellent agreement with equation (3.3). Simulations with $w_1 > w_2$ are not included in the fit as they are predicted to satisfy a different scaling. We conclude the theory of spreading speeds in a current sheet varying in thickness from w_1 to w_2 is accurate.

We use the same simulations to test our prediction for spreading in current sheets with a thickness that varies continuously in the out-of-plane direction. To compare with equation (3.12), we estimate the spreading timescale in the region where the current sheet thickness changes in the simulation with $(w_1, w_2) = (1, 2)$. The stack plot for the simulation in Fig. 5.6(d) shows that reconnection spreads across the region $-84 < z < -76$ approximately over the time range $100 < t <$

120, so $\tau \simeq 20$. From equation (4.1), the thickness varies approximately linearly across the transition region $-84 < z < -76$, so we use $\alpha = 1$ and $\Delta z = 2w_z = 8$. Using equation (3.12), the spreading time across the region where the current sheet thickness changes is predicted to be $\tau \approx 19$. This is in good agreement with the simulation results. To further test the theory, two additional simulations with $(w_1, w_2) = (1, 2)$ are performed using $w_z = 8$ and $w_z = 12$ for the gradient length scale in equation (4.1), doubling and tripling Δz. The spreading timescales in the higher w_z simulations increase approximately by factors of 2 and 3, respectively (not shown). This is in agreement with the predicted scaling with Δz in equation (3.12) assuming the same linear profile with $\alpha = 1$. These results suggest that the theory for the spreading speed in current sheets with a gradually varying thickness is valid.

(w_1, w_2)	Predicted v_{s2}	Measured v_{s2}	Deviation
(1.0,1.0)	1.00	0.97	-3.1%
(2.0,2.0)	0.50	0.51	2.0%
(1.9,2.0)	0.48	0.41	-15.9%
(1.75,2.0)	0.44	0.38	-15.1%
(1.5,2.0)	0.38	0.31	-21.0%
(1.0,2.0)	0.25	0.29	13.8%
(0.75,2.0)	0.19	0.26	-27.9%
(1.0,1.25)	0.64	0.68	5.9%
(1.0,1.5)	0.44	0.52	14.5%
(1.0,1.75)	0.33	0.37	11.7%
(2.25,2.0)	0.50	0.46	-8.0%
(2.5,2.0)	0.50	0.51	2.0%
(2.0,1.5)	0.67	0.73	9.5%

Table 5.4 Results for 3D two-fluid simulations in this study. The first column gives ordered pairs (w_1, w_2) for current sheets that vary in half-thickness along the out-of-plane direction from a value of w_1 to w_2 in units of d_{i0}. v_{s2} is the reconnection spreading speed in the region with half-thickness w_2. The second column gives the theoretical predictions from Chapter 3, and the third column gives the values measured from the simulations. The deviation from the theory is shown as a percentage in the fourth column.

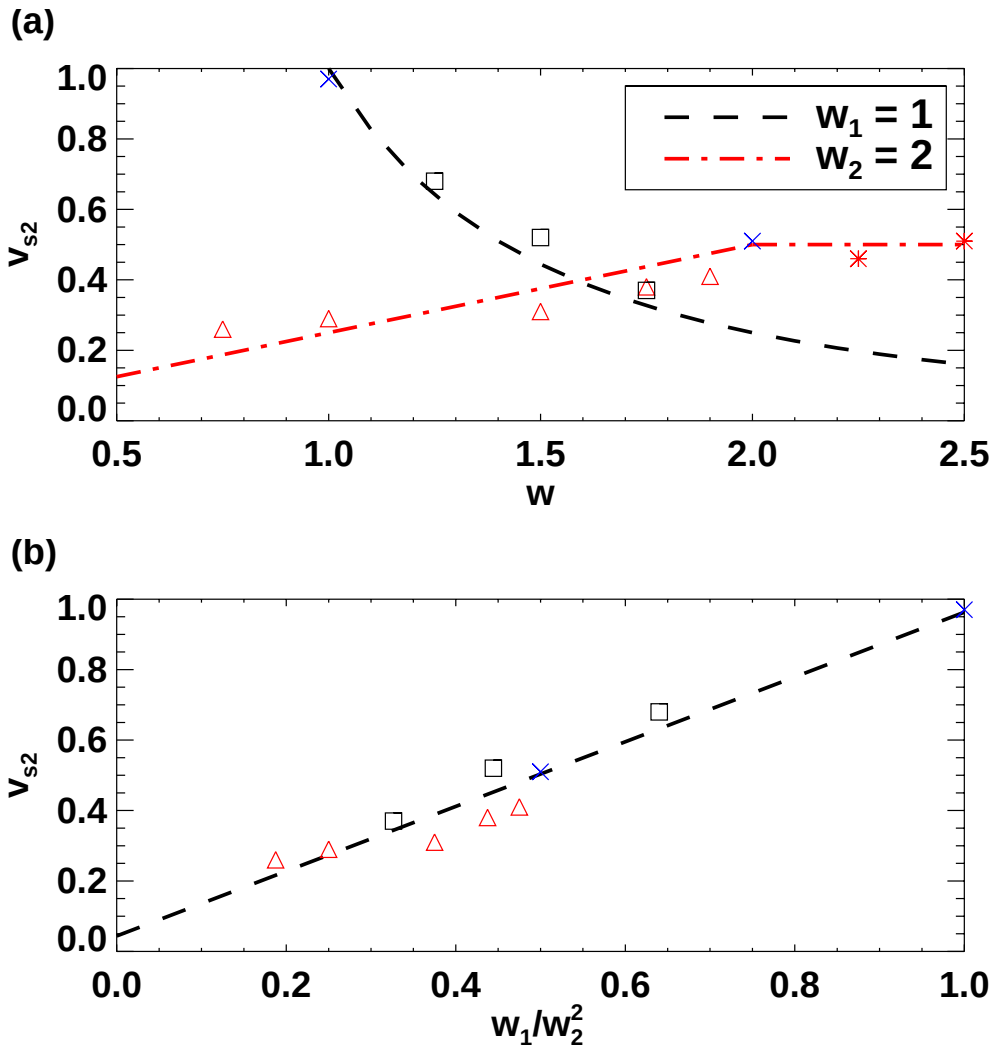

Figure 5.7 Comparison of simulation results and theory for the reconnection spreading speed v_{s2} in units of c_{A0} in the region where the initial current sheet half-thickness is w_2 in units of d_{i0} for anti-parallel reconnection simulations with current sheets that vary in the out-of-plane direction from a half-thickness w_1 to w_2. (a) v_{s2} as a function of the current sheet half-thickness w, which represents either independent variable w_1 or w_2, depending on which is the independent variable for the given set of simulations. Two uniform half-thickness simulations $(w_1, w_2) = (1, 1)$ and (2, 2) are shown as blue crosses. Three simulations with $w_1 = 1$ and $w_2 = 1.25$, 1.5, 1.75 are shown as black squares and the independent variable is $w = w_2$. Five simulations with $w_1 = 0.75$, 1.0, 1.25.1.5, 1.75, 1.9 and $w_2 = 2$ are shown as red triangles and two simulations with $w_1 = 2.25$, 2.5 and $w_2 = 2$ are shown as red asterisks, where the independent variable is $w = w_1$. The dashed black line represents the theoretical prediction from equation (3.3) for simulations with $w_1 = 1$ fixed with $w = w_2$ as the independent variable. The red dash-dot piecewise-curve represents the prediction from equation (3.3) with $w_2 = 2$ fixed with $w = w_1$ as the independent variable for $w_1 < w_2$, and equation (3.7) for $w_1 > w_2$. (b) v_{s2} as a function of w_1/w_2^2 for simulations with $w_1 \leq w_2$. The dashed black line gives the theoretical prediction from equation (3.3).

Chapter 6

Applications

We now discuss some applications of the theory of anti-parallel reconnection spreading in developed in Chapter 3.

6.1 Reconnection Spreading in the Near-Earth Magnetotail

The central plasma sheet in the near-Earth magnetotail is known to vary in thickness continuously in the dawn-dusk direction Y_{GSM} in the Geocentric Solar Magnetospheric (GSM) coordinate system, equivalent to the z coordinate in Chapter 2. It has a minimum thickness at midnight magnetic local time and maxima at the flanks near the nightside magnetopause [see Fig. 1.10 in Sec. 1.4 and Fig. 7 in Tsyganenko (1998)]. The anti-parallel field configuration and low collisionality makes it an ideal system to apply the theory in Sec. 3.4.

First, we estimate the timescale for magnetic reconnection to spread during a substorm expansion event in the near-Earth magnetotail. For pre-substorm initial conditions, assuming a fully ionized hydrogen plasma, a reconnecting magnetic field with an asymptotic value $B_x \approx 20$ nT (Miyashita et al., 2020) and a magnetosphere density at the plasma sheet boundary layer of $n \approx 0.1$ cm^{-3} (Baumjohann et al., 1990), we estimate the ion inertial scale is $d_i \approx 720$ km and the Alfvén speed is $c_A \approx 1400$ km s^{-1}. We take $w_1 \approx 0.1 - 0.4 R_E \approx 0.89 - 3.5\ d_i$ as the minimum

cross-tail half-thickness at midnight and $w_2 \approx 1R_E \approx 8.9\ d_i$ as the maxima at the flanks, and $\Delta z \sim 15R_E \approx 133d_i$ as the approximate half-length of the cross-tail current sheet along the dawn-dusk direction (Fairfield, 1980; Sergeev et al., 1990). Since Δz greatly exceeds the ion inertial scale, the assumption that the current sheet only gradually becomes thicker is valid. We assume reconnection begins with a finite x-line with its dawnward edge situated at midnight ($Y_{GSM} = 0$), such that reconnection spreads dawnwards in the direction of electron motion (Nagai et al., 2011, 2013) until reaching $Y_{GSM} = -\Delta z = -15R_E$. Assuming a parabolic cross-tail current sheet, we use $\alpha = 2$ in equation (3.11). Using equation (3.12), this gives spreading timescales in the range $\tau \approx 2.5 - 23.6$ minutes, where the range depends on the value for w_1. For comparison, if the cross-tail current sheet were uniform with a typical midnight half-thickness $w_1 \approx 0.1 - 0.4\ R_E \approx 0.89 - 3.5\ d_i$, equation (3.1) implies the timescale for spreading would be in the range of $\tau \approx 1 - 4$ minutes, comparable to the Alfvén crossing time $\approx$ 1 minute. Thus the theory provides a mechanism for reconnection spreading along the cross-tail current sheet on timescales longer than both what Alfvén and current carrier speeds suggest.

Observations suggest that reconnection in the near-Earth magnetotail may begin with an x-line with its dawnward edge at $Y_{GSM} > 0$ (Nagai et al., 2013). This implies reconnection first spreads from a thicker part of the current sheet into the thinner part at midnight before continuing to spread dawnwards towards a thicker part of the current sheet. In this scenario, the timescale for spreading in the $Y_{GSM} > 0$ region would be calculated with equation (3.13) for spreading along the region of decreasing current sheet thickness.

There is also observational evidence that reconnection may not spread across the entire dawn-dusk direction, instead stopping when the x-line is $\sim 8R_E$ in length (Nagai et al., 2013). Constraining Δz to empirical values in equations (3.12) and (3.13) may give more accurate predictions. We point out that the structure of the cross-tail current sheet may also be more complex and bend away from the dawn-dusk direction asymmetrically near the flanks due to seasonal and diurnal oscillations of Earth's dipole tilt angle (Tsyganenko, 1998). This effect is not captured in our model current sheet, but it is reasonable to expect that if the radius of curvature of the plasma sheet is much larger than the ion inertial scale that it would introduce only small corrections to the present results.

6.2 Reconnection Spreading in Two-Ribbon Solar Flares

Another scenario where the theory may be applicable is in the spreading or "zipper" motion of the ribbons in two-ribbon flares, which is thought to result from out-of-plane spreading of magnetic reconnection in the solar corona [see Qiu et al. (2010); Tian et al. (2015); Qiu et al. (2017) and references therein]. Qiu et al. (2017) analyzed six two-ribbon flare events that show ribbon elongation/spreading occurs at speeds typically slower than the coronal Alfvén speed by as much as an order of magnitude. One previously known mechanism that could explain a sub-Alfvénic reconnection spreading speed is that the current sheet could have uniform thickness but be thicker than ion inertial scales (Shay et al., 2003; Arencibia et al., 2021). This may be a potential explanation for unidirectional spreading of ribbons with a

uniform speed in flare events with a weak guide field, such as in Fig. 5 in Qiu et al. (2017).

The results of the present study provide another mechanism for spreading speeds below the Alfvén speed. An observational signature of this scenario is a reconnection spreading speed that slows with distance. Additionally, if the minimum and maximum half-thicknesses w_1 and w_2 are both larger than the ion inertial scale, the spreading speed is predicted to be both sub-Alfvénic and below the local current carrier speed at any location in the current sheet. This is qualitatively similar to the behavior of observed ribbon elongation speeds in Fig. 2 in Qiu et al. (2017) and Fig. 9 in Naus et al. (2022), both showing ribbon elongation speeds varying along the direction of spreading, although we note the former is for an event in which the flare ribbons spread in the direction opposite to that of the inferred current carriers. This signature may potentially be useful for inferring the structure of a reconnecting coronal current sheet as has been alluded to in Naus et al. (2022), even though the thicknesses in question are far below currently resolvable scales in the corona ($d_i \sim 10$ m).

Chapter 7

Summary of Work

7.1 Advances to the Basic Understanding of Magnetic Reconnection Spreading

We study the out-of-plane spreading of 3D magnetic reconnection that begins localized in the out of plane z direction. We build off of a previously developed analysis (Huba & Rudakov, 2002) for the spreading of anti-parallel collisionless reconnection. It describes the unidirectional spreading as caused by electrons convecting the reconnected magnetic field out of the reconnection plane (which they dubbed a "reconnection wave"), and quantified by the Hall term in the electron-MHD induction equation. In this dissertation, we re-envision the previous model using a scaling analysis of Faraday's law using the full generalized Ohm's law rather than a linear analysis. We show that the same analytical approach can be used in a unified manner to describe the spreading of collisionless reconnection with a guide field, resulting in the known spreading speed given by the Alfvén speed and spreading bidirectionally (Katz et al., 2010; Shepherd & Cassak, 2012). The same approach also provides an explanation for why anti-parallel reconnection in resistive-MHD does not spread (Nakamura et al., 2012).

Importantly, this new interpretation provides an alternate, first-principles un-

derstanding of the mechanism of reconnection spreading. In this approach, reconnection spreading occurs when the x-line extends, which requires the seeding of an x-line in the non-reconnecting region [see also Jain et al. (2013)]. Thus, if the normal (y) component of the magnetic field is induced in a way that produces an x-line topology, then reconnection spreads. The normal magnetic field subsequently grows in time due to the tearing instability [see also Li et al. (2020)] until steady-state reconnection is reached, with some time delay after B_y enters the region previously not undergoing reconnection. If no x-line topology is induced at the interface between reconnecting and non-reconnecting regions, then the x-line does not spread in that direction. The induction of the normal magnetic field is controlled by the out of plane gradient of the component of the electric field in the outflow direction (x). For anti-parallel reconnection in which electrons carry the current, the Hall term dominates the E_x contribution due to electron convection. For reconnection with a strong guide field, spreading is caused by the bending of the upstream magnetic field, which occurs predominantly at the boundary between the reconnecting and non-reconnecting regions. This sets up a strong magnetic curvature force driving flows in the y direction. There is an associated electric field E_x due to convection v_y through the guide field B_z, which induces the necessary B_y to produce an x-line topology in both directions. This mechanism relies only on MHD physics, showing that collisional guide field reconnection can spread similar to collisionless guide field reconnection.

The analysis carried out here makes it clear that spreading with and without a guide field are dominated by different physics. Consequently, the MHD description is

sufficient to describe the speed and bidirectionality of the spreading in reconnection with a strong guide field. In contrast, the MHD description does not properly describe the spreading of anti-parallel reconnection, at least for the uniform resistivity profile employed in the present study. Our analytical findings reveal that collisions can in principle cause reconnection to spread bidirectionally at the diffusion speed, which could be important for collisional reconnection in the laboratory and some settings in the Sun. This has important implications for global 3D modeling in coronal and magnetospheric settings. Global MHD simulations have historically been quite common in both settings. Our results suggest that care is needed when the reconnection is anti-parallel in such settings. In most settings where collisionality is quite weak, our model suggests collisions play no important role in reconnection spreading. We confirm the validity of each of these analytical results using 3D two-fluid and resistive MHD numerical simulations.

The theory presented here assumes reconnection spreads solely by inducing the x-line topology in non-reconnecting regions. An alternate model is that a pressure minimum in the reconnecting region is convected into the non-reconnecting region, generating an inflow to initiate reconnection and thus elongate the x-line (Huba & Rudakov, 2003; Nakamura et al., 2012; Dorfman et al., 2013). We note this model would predict that anti-parallel reconnection in resistive MHD would convect at the speed of the current carriers. However, numerical simulations in this work and in Nakamura et al. (2012) show no evidence of this. This suggests that induction of the reconnecting magnetic field in the out of plane direction, not the pressure gradient between reconnecting and non-reconnecting regions, is the essential ingredient for

spreading.

7.2 New Knowledge from the Numerics

Our simulation study also reveals two other important aspects of reconnection spreading. First, we find that in current sheets wider than the ion inertial scale (for current sheets up to thicknesses of $3d_i$), reconnecting x-lines continually grow in length. This differs from prior work in which reconnection x-lines convected with a fixed extent without spreading (Shay et al., 2003; Meyer III, 2013). We hypothesize that the reason for the difference is that the prior work employed a computational domain with a square reconnecting geometry, while ours employ a rectangular geometry. The difference is likely caused by the additional free magnetic energy in the rectangular domain. Assessing this more carefully should be the subject of future research. Second, our simulation of anti-parallel reconnection with a perturbation in the plasma pressure to force reconnection instead of using a magnetic perturbation still results in reconnection spreading with the direction and speed of the current carriers. It does not spread at the faster magnetosonic speed, as has been previously postulated (Vorpahl, 1976). Future research with other simulation setups are needed to more thoroughly test this prediction.

7.3 New Theory of Reconnection Spreading in Current Sheets of Non-Uniform Thickness

We also extend the model of anti-parallel reconnection to systems with current sheet thicknesses that vary in the out-of-plane direction. Existing theories only apply to current sheets of uniform thickness, predicting that anti-parallel collisionless reconnection spreads at the speed of the local current carriers in the sheet, $v_s = c_A(d_i/w_2)$ for a current sheet of uniform half-thickness w_2, where c_A is the Alfvén speed based on the reconnecting field and d_i is the ion inertial length. However, real systems undergoing reconnection such as solar flares, Earth's magnetotail or dayside magnetopause are unlikely to be made up of uniform thickness current sheets. The theory here can be used to understand spreading in such systems. For non-uniform thickness sheets with an abrupt change from a half-thickness w_1 to a greater half-thickness w_2, we predict that the spreading speed is reduced to $v_s = c_A(w_1 d_i/w_2)^2$, slower than of the local current carrier speed by a factor of w_1/w_2, due to a reduction in the initial effective reconnecting magnetic field strength (Shay et al., 2004). Therefore, there is a memory effect from the region from which reconnection starts, a departure from existing knowledge and a key prediction of the theory. Importantly, our result provides a mechanism for reconnection spreading slower than the Alfvén and current carrier speeds, which has been inferred from observations in both the solar and magnetospheric settings. For spreading from a thicker to thinner current sheet, the spreading speed is the speed of the current carriers, $v_s = c_A(d_i/w_2)$, so there is no memory effect from the region that reconnection begins.

For a current sheet where the change in thickness is gradual (compared to the ion inertial scale), the results from the analysis in Sec. 3.4 above carry over as the instantaneous speed based on the local thickness $w(z)$. This allows for a calculation for the time-scale of reconnection spreading in a current sheet with a known profile for $w(z)$.

We apply the theory of spreading in current sheets of non-uniform thickness to the near-Earth magnetotail during active times, a scenario where the thickness of the near-Earth cross-tail current sheet increases continuously from midnight out to the flank magnetopause. Using a model magnetotail current sheet profile for $w(z)$, We find the theory gives plausible time-scales on the order of 20 minutes for reconnection spreading across approximately the entire length of the cross-tail current sheet. Such an analysis could also be employed for quiet time events, but this was not carried out in this study. Both predictions should be able to be compared with direct or remote observations, which would be an important step for future work.

In two-ribbon solar flares, our scaling of spreading speeds in current sheets of non-uniform thickness may potentially explain why the ribbons in events with nearly anti-parallel reconnecting fields may spread at sub-Alfvénic speeds. Moreover, we provide an observational signature for spreading in a current sheet with a varying thickness, *i.e.,* that the speeds change in time during the spreading process. The inferred current sheet thicknesses remain far below current observational capacities, so other approaches will be necessary to confirm or refute the model in solar flares.

7.4 Limitations of This Study

Our simulations assume the asymptotic reconnecting magnetic field strength is the same everywhere along the current sheet, but this need not be the case. We expect that the results here would carry over with B_0 replaced by $B_x(z)$ in such a scenario, but future work would be required to test this hypothesis. Simulations in a 3D box geometry may leave out important geometrical effects from realistic systems, including curvature of the magnetic fields and density structure in the solar corona, as well as curvature of the near-Earth magnetotail current sheet during seasonal and diurnal oscillations of Earth's dipole tilt angle and the normal $B_{z,GSM}$ present in the near-Earth magnetotail.

Our study of spreading in current sheets of non-uniform thickness does not include an out-of-plane (guide) magnetic field, which may be relevant in solar flare ribbon spreading events and for the dayside magnetopause and the solar wind where guide fields may be significant.

The simulations in this study employ cold electrons within the two-fluid model, so drift waves are absent. In a realistic system, drift waves are expected to potentially be excited where there is a change in the current sheet thickness in the out-of-plane direction. The effect might be expected to be small if the current sheet thickness changes over length scales larger than the electron inertial scale, but studying whether drift waves impact the spreading speed should be the subject of future work.

For applications to the corona or magnetosphere, simulations in a 3D box may

not faithfully capture the geometry of the system, including plasma and magnetic field asymmetries at the dayside magnetopause (Li et al., 2020), curvature of the large-scale magnetic fields, and density stratification in the corona. As has been previously pointed out (Qiu et al., 2017), some two-ribbon flare spreading events with nearly anti-parallel magnetic fields spread in the direction opposite to that of the inferred current carriers. This may be related to the global magnetic field configuration not captured in the treatment here. More work is needed to understand spreading in fundamentally 3D reconnection geometries (Lukin & Linton, 2011).

7.5 Future Outlook for the Field

There are many avenues for future studies based on this work. Our result may be important in the context of recent findings that the spreading of asymmetric guide field reconnection at Earth's dayside magnetopause occurs at Alfvénic speeds bidirectionally for thin current sheets (Zou et al., 2018; Li et al., 2020), but at the slower speed of the current carriers for thicker current sheets. They argued that the reason is that the tearing instability is slower in thicker current sheets, and showed this hypothesis organizes when the spreading is Alfvénic or dominated by current carriers. Then, information about the onset time [alternately the growth time of the linear tearing mode (Li et al., 2020)] is needed to find the time until reconnection onsets. If too slow, other spreading mechanisms could be faster. In particular, the present analysis suggests that different spreading mechanisms are additive, so convection of the reconnected magnetic field by the current carriers

remains an active effect due to the Hall term in the generalized Ohm's law even if the convection term that drives spreading in thin current sheets is small for thicker current sheets. More research is needed to understand the interplay between the multiple possible spreading mechanisms.

Also, as discussed earlier, it is important to study the relationship between the reconnection region spreading vs. convecting as a function of system parameters, including the computational domain size, the perturbation size and wavenumber (Jain et al., 2013), the current sheet thickness, and when the gradient in the thickness of the current sheet is very large (Huang et al., 2020). Further work is also needed to understand how the spreading is impacted by the mechanism that reconnection is seeded, especially with a guide field. As anomalous resistivity has been invoked to explain reconnection in the solar corona (Ugai & Tsuda, 1977; Sato & Hayashi, 1979), it is also important to study spreading with this dissipation mechanism.

An extension of our results to asymmetric reconnection may also be useful for the study of reconnection spreading at the dayside magnetopause, where it has been reported that the spreading speed of reconnection is sub-Alfvénic (Zou et al., 2018). Preliminary simulations of 3-D anti-parallel Hall reconnection carried out but not included in this dissertation show a complicated dependence of the spreading velocity on asymmetric reconnecting fields and densities, indicating a careful analytical study of the effect that asymmetries have on reconnection spreading is warranted.

Bibliography

Alfvén, H. 1942, Nature, 150, 405

Arencibia, M., Cassak, P. A., Shay, M. A., & Priest, E. R. 2021, Physics of Plasmas, 28, 082104. https://doi.org/10.1063/5.0052189

Arencibia, M., Cassak, P. A., Shay, M. A., et al. 2022, submitted

Axford, W. I. 1984, in Magnetic Reconnection in Space and Laboratory Plasmas, ed. J. Edward W. Hones, Geophysical Monograph 30 (American Geophysical Union), 1–8

Baumjohann, W., Paschmann, G., & Luhr, H. 1990, Journal of Geophysical Research-Space Physics, 95, 3801

Bessho, N., & Bhattacharjee, A. 2005, Phys. Rev. Lett., 95, 245001

Birn, J., & Priest, E., eds. 2007, Reconnection of Magnetic Fields (Cambridge University Press)

Birn, J., Drake, J. F., Shay, M. A., et al. 2001, J. Geophys. Res., 106, 3715

Biskamp, D. 1986, Phys. Fluids, 29, 1520

Carmichael, H. 1964, in AAS/NASA Symposium on the Physics of Solar Flares, ed. W. N. Ness (NASA, Washington, DC), 451

Cassak, P. A., & Drake, J. F. 2009, Ap. J. Lett., 707, L158

Chacón, L., Simakov, A., Lukin, V. S., & Zocco, A. 2008, Phys. Rev. Lett., 101, 025003

Cheng, J. X., Kerr, G., & Qiu, J. 2011, ApJ, 744, 48. https://doi.org/10.1088/0004-637x/744/1/48

Choudhuri, A. R. 1998, The Physics of Fluids and Plasmas (Cambridge University Press)

Cothran, C. D., Landreman, M., Brown, M. R., & Matthaeus, W. H. 2005, Geophys. Res. Lett., 32, L03105

Cowley FRS, S. W. H. 2015, in Magnetospheric Plasma Physics: The Impact of Jim Dungey's Research, ed. S. W. H. Cowley FRS, D. Southwood, & S. Mitton (Cham: Springer International Publishing), 1–32

Daughton, W., & Karimabadi, H. 2007, Phys. Plasmas, 14, doi:10.1063/1.2749494

Dorfman, S., Ji, H., Yamada, M., et al. 2013, Geophys. Res. Lett., 40, 1

—. 2014, Physics of Plasmas, 21, 012109. https://aip.scitation.org/doi/10.1063/1.4862039

Drake, J. F., Shay, M. A., Thongthai, W., & Swisdak, M. 2005, Phys. Rev. Lett., 94, 095001

Drake, J. F., Swisdak, M., Schoeffler, K. M., Rogers, B. N., & Kobayashi, S. 2006, Geophys. Res. Lett., 33, L13105

Dungey, J. W. 1953, Phil. Mag., 44, 725

—. 1958, Cosmic Electrodynamics (Cambridge University Press)

—. 1961, Phys. Rev. Lett., 6, 47

Eastwood, J., Nakamura, R., Turc, L., Mejnertsen, L., & Hesse, M. 2017, The Scientific Foundations of Forecasting Magnetospheric Space Weather, 339–370

Egedal, J., Katz, N., Bonde, J., et al. 2011, Phys. Plasmas, 18, 111203

Fairfield, D. H. 1979, Journal of Geophysical Research: Space Physics, 84, 1950. https://agupubs.onlinelibrary.wiley.com/doi/abs/10.1029/JA084iA05p01950

—. 1980, Journal of Geophysical Research, 85, 775

Furth, H. P., Killeen, J., & Rosenbluth, M. N. 1963, Phys. Fluids, 6, 459

Giovanelli, R. G. 1950, Ph. D. Thesis

Gosling, J. T., Skoug, R. M., McComas, D. J., & Smith, C. W. 2005, J. Geophys. Res., 110, doi:10.1029/2004JA010809

Gosling, J. T., Thomsen, M. F., Bame, S. J., Elphic, R. C., & Russell, C. T. 1990, J. Geophys. Res., 95, 8073

Gosling, J. T., Eriksson, S., Blush, L. M., et al. 2007, Geophys. Res. Lett., 34, L20108

Graham, D. R., & Cauzzi, G. 2015, ApJL, 807, L22

Guzdar, P. N., Drake, J. F., McCarthy, D., Hassam, A. B., & Liu, C. S. 1993, Phys. Fluids B, 5, 3712

Hesse, M., Kuznetsova, M., & Birn, J. 2001, J. Geophys. Res., 106, 29831

Hesse, M., Schindler, K., Birn, J., & Kuznetsova, M. 1999, Phys. Plasmas, 6, 1781

Hietala, H., Eastwood, J. P., & Isavnin, A. 2014, Plasma Phys. Control. Fusion, 56, 064011

Hirayama, T. 1974, Solar Phys., 34, 323

Huang, K., Liu, Y.-H., Lu, Q., & Hesse, M. 2020, Geophysical Research Letters, 47, e2020GL088147, e2020GL088147 10.1029/2020GL088147. https://agupubs.onlinelibrary.wiley.com/doi/abs/10.1029/2020GL088147

Huba, J. D., & Rudakov, L. I. 2002, Phys. Plasmas, 9, 4435

—. 2003, Phys. Plasmas, 10, 3139

Isobe, H., Yokoyama, T., Shimojo, M., et al. 2002, Ap. J., 566, 528

Jain, N., & Büchner, J. 2017, Physics of Plasmas, 24, 082304

Jain, N., Büchner, J., Dorfman, S., Ji, H., & Sharma, A. S. 2013, Phys. Plasmas, 20, 112101

Jain, N., Büchner, J., Comişel, H., & Motschmann, U. 2021, The Astrophysical Journal, 919, 103. https://doi.org/10.3847/1538-4357/ac106c

Karimabadi, H., Krauss-Varban, D., Huba, J. D., & Vu, H. X. 2004, J. Geophys. Res., 109, A09205

Katz, N., Egedal, J., Fox, W., et al. 2010, Phys. Rev. Lett., 104, 255004

Kaymaz, Z., Siscoe, G., Tsyganenko, N., & Lepping, R. 1994, Journal of Geophysical Research, 99, 8705

Kivelson, M. G., & Russell, C. T., eds. 1995, Introduction to Space Physics (Cambridge University Press)

Kleva, R., Drake, J., & Waelbroeck, F. 1995, Phys. Plasma, 2, 23

Kopp, R. A., & Pneuman, G. W. 1976, Solar Phys., 50, 85

Lapenta, G., Krauss-Varban, D., Karimabadi, H., et al. 2006, Geophys. Res. Lett., 33, L10102

Lee, J., & Gary, D. E. 2008, ApJ, 685, L87

Li, T., Liu, Y.-H., Hesse, M., & Zou, Y. 2020, Journal of Geophysical Research: Space Physics, 125, e2019JA027094

Linton, M. G., & Longcope, D. W. 2006, Ap. J., 642, 1177

Liu, C., Lee, J., Jing, J., et al. 2010, ApJL, 721, L193. https://doi.org/10.1088/2041-8205/721/2/l193

Liu, Y.-H., Cassak, P., Li, X., et al. 2022, Communications Physics, 5, 97

Liu, Y.-H., Daughton, W., Karimabadi, H., Li, H., & Peter Gary, S. 2014, Physics of Plasmas, 21, 022113. https://doi.org/10.1063/1.4865579

Liu, Y.-H., Hesse, M., Guo, F., et al. 2017, Phys. Rev. Lett., 118, 085101

Liu, Y.-H., Li, T. C., Hesse, M., et al. 2019, J. Geophys. Res., arXiv:1901.10195

Lockwood, M. 2016, Space Weather, 14, 380. https://agupubs.onlinelibrary.wiley.com/doi/abs/10.1002/2016SW001438

Lukin, V. S., & Linton, M. G. 2011, Nonlinear Processes in Geophysics, 18, 871

Mandt, M. E., Denton, R. E., & Drake, J. F. 1994, Geophys. Res. Lett., 21, 73

McPherron, R. L. 1970, J. Geophys. Res., 75, 5592

McPherron, R. L., Russell, C. T., & Aubry, M. P. 1973, J. Geophys. Res., 78, 3131

Meyer III, J. C. 2013, PhD thesis, University of Delaware

Miyashita, Y., Seki, K., Sakaguchi, K., et al. 2020, Journal of Geophysical Research: Space Physics, 125, e2019JA027561

Nagai, T. 1982, J. Geophys. Res., 87, 4405

Nagai, T., Shinohara, I., Fujimoto, M., et al. 2011, Journal of Geophysical Research: Space Physics, 116, https://agupubs.onlinelibrary.wiley.com/doi/pdf/10.1029/2010JA016283. https://agupubs.onlinelibrary.wiley.com/doi/abs/10.1029/2010JA016283

Nagai, T., Shinohara, I., Zenitani, S., et al. 2013, Journal of Geophysical Research: Space Physics, 118, 1667. https://agupubs.onlinelibrary.wiley.com/doi/abs/10.1002/jgra.50247

Nakamura, T. K. M., Nakamura, R., Alexandrova, A., Kubota, Y., & Nagai, T. 2012, J. Geophys. Res., 117, 03220

Naus, S. J., Qiu, J., DeVore, C. R., et al. 2022, ApJ, 926, 218

Parker, E. N. 1957, J. Geophys. Res., 62, 509

Petschek, H. E. 1964a, in AAS/NASA Symposium on the Physics of Solar Flares, ed. W. N. Ness (NASA, Washington, DC), 425

Petschek, H. E. 1964b, in NASA-SP, Vol. 50, Proc. AAS-NASA Symp. Phys. Solar Flares, 425–439

Phan, T. D., Gosling, J. T., Davis, M. S., et al. 2006, Nature, 439, 175

Pontin, D. I. 2011, Adv. Space Res., 47, 1508

Priest, E., & Forbes, T. 2000, Magnetic Reconnection (Cambridge University Press)

Pritchett, P. L., & Coroniti, F. V. 2004, J. Geophys. Res., 109, 1220,doi10.1029/2003JA009999

Pyakurel, P. S., Shay, M. A., Drake, J. F., et al. 2021, Phys. Rev. Lett., 127, 155101. https://link.aps.org/doi/10.1103/PhysRevLett.127.155101

Qiu, J. 2009, Ap. J., 692, 1110

Qiu, J., Liu, W., Hill, N., & Kazachenko, M. 2010, Ap. J., 725, 319

Qiu, J., Longcope, D. W., Cassak, P. A., & Priest, E. R. 2017, ApJ, 838, 17

Reeves, K. K., Guild, T. B., Hughes, W. J., et al. 2008, Journal of Geophysical Research: Space Physics, 113, https://agupubs.onlinelibrary.wiley.com/doi/pdf/10.1029/2008JA013049. https://agupubs.onlinelibrary.wiley.com/doi/abs/10.1029/2008JA013049

Ren, Y., Yamada, M., Gerhardt, S., et al. 2005, Phys. Rev. Lett., 95, 005003

Rogers, B. N., Denton, R. E., Drake, J. F., & Shay, M. A. 2001, Phys. Rev. Lett., 87, 195004

Russell, A. J. B., Yeates, A. R., & Eastwood, J. P. 2015, Astronomy Geophysics, 56, 6.18. https://doi.org/10.1093/astrogeo/atv197

Sasunov, Y. L., Semenov, V. S., Heyn, M. F., et al. 2015, Journal of Geophysical Research (Space Physics), 120, 8194

Sato, T., & Hayashi, T. 1979, Phys. Fluids, 22, 1189

Sergeev, V. A., Tanskanen, P., Mursula, K., Korth, A., & Elphic, R. C. 1990, , 95, 3819

Shay, M. A., Drake, J. F., Rogers, B. N., & Denton, R. E. 1999a, Geophys. Res. Lett., 26, 2163

—. 1999b, Geophys. Res. Lett., 26, 2163

Shay, M. A., Drake, J. F., Swisdak, M., Dorland, W., & Rogers, B. N. 2003, Geophys. Res. Lett., 30, 1345

Shay, M. A., Drake, J. F., Swisdak, M., & Rogers, B. N. 2004, Phys. Plasmas, 11, 2199

Shepherd, L. S., & Cassak, P. A. 2012, J. Geophys. Res., 117, A10101

Shepherd, L. S., Cassak, P. A., Drake, J. F., et al. 2017, Ap. J., 848, 90

Shibata, K., Masuda, S., Shimojo, M., et al. 1995, ApJL, 451, L83

Slavin, J. A., Imber, S. M., & Raines, J. M. 2021, A Dungey Cycle in the Life of Mercury's Magnetosphere (American Geophysical Union (AGU)), 535–556. https://agupubs.onlinelibrary.wiley.com/doi/abs/10.1002/9781119815624.ch34

Sturrock, P. A. 1966, Nature, 211, 695

Sweet, P. A. 1958, in Electromagnetic Phenomena in Cosmical Physics, ed. B. Lehnert (Cambridge University Press, New York), 123

Tian, H., Young, P. R., Reeves, K. K., et al. 2015, ApJ, 811, 139

Tripathi, D., Isobe, H., & Mason, H. E. 2006, Astron. Astrophys., 453, 1111

Tsyganenko, N. A. 1998, , 103, 23551

Ugai, M., & Tsuda, T. 1977, J. Plasma Phys., 17, 337

Vasyliunas, V. M. 1975, Rev. Geophys., 13, 303

Voigt, G. H. 1984, , 89, 2169

Vorpahl, J. A. 1976, ApJ, 205, 868

Walsh, B. M., Welling, D. T., Zou, Y., & Nishimura, Y. 2018, Geophysical Research Letters, 45, 5268. https://agupubs.onlinelibrary.wiley.com/doi/abs/10.1029/2018GL078230

Zhou, M., Ashour-Abdalla, M., Deng, X., et al. 2017, Journal of Geophysical Research (Space Physics), 122, 9513

Zou, Y., Walsh, B. M., Nishimura, Y., et al. 2018, , 45, 80

Zou, Y., Walsh, B. M., Nishimura, Y., et al. 2018, Geophysical Research Letters, 45, 80. https://agupubs.onlinelibrary.wiley.com/doi/abs/10.1002/2017GL075765

—. 2019, Annales Geophysicae, 37, 215. https://angeo.copernicus.org/articles/37/215/2019/